Architecture of the yeast Pol III pre-termination complex and pausing mechanism on poly(dT) termination signals

Mathias Girbig, Juanjuan Xie, Helga Grötsch, Domenico Libri, Odil Porrua, Christoph Müller

Cell Reports

Article

Architecture of the yeast Pol III pre-termination complex and pausing mechanism on poly(dT) termination signals

Graphical abstract

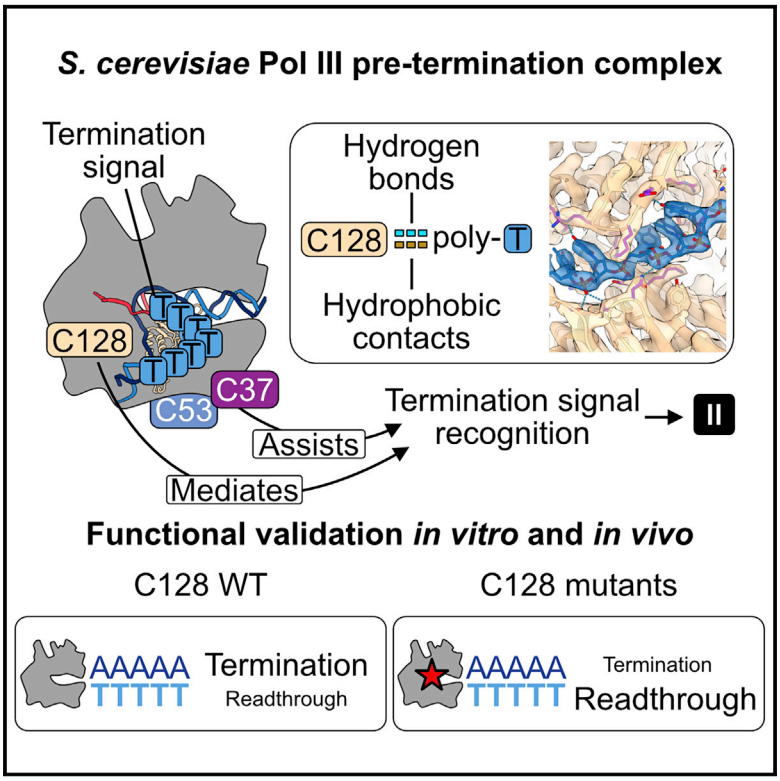

Highlights

- We report the cryo-EM structure of the yeast RNA polymerase III pre-termination complex
- Polar interactions between subunit C128 and the poly(dT) termination site induce pausing
- Mutating key interaction residues in C128 impairs termination *in vitro* and *in vivo*
- Subcomplex C53-C37 does not bind poly(dT) but assists in its recognition through C128

Authors

Mathias Girbig, Juanjuan Xie, Helga Grötsch, Domenico Libri, Odil Porrua, Christoph W. Müller

Correspondence

christoph.mueller@embl.de

In brief

RNA polymerase III (Pol III) terminates transcription of small RNAs on polythymine sequences on the non-template DNA strand. Girbig et al. report and functionally validate the structure of the yeast Pol III pre-termination complex, thereby revealing how termination signal recognition and transcription pausing, a critical prerequisite for termination, is achieved.

Girbig et al., 2022, Cell Reports *40*, 111316
September 6, 2022
https://doi.org/10.1016/j.celrep.2022.111316

CellPress

Cell Reports

CellPress
OPEN ACCESS

Article

Architecture of the yeast Pol III pre-termination complex and pausing mechanism on poly(dT) termination signals

Mathias Girbig,[1,3] Juanjuan Xie,[2,4] Helga Grötsch,[1,5] Domenico Libri,[2,6] Odil Porrua,[2,6] and Christoph W. Müller[1,7,*]
[1]Structural and Computational Biology Unit, European Molecular Biology Laboratory (EMBL), Meyerhofstraße 1, 69117 Heidelberg, Germany
[2]Université de Paris, CNRS, Institut Jacques Monod, 75006 Paris, France
[3]Present address: Max Planck Institute for Terrestrial Microbiology, Karl-von-Frisch Straße 10, 35043 Marburg, Germany
[4]Present address: Cold Spring Harbor Laboratory, Cold Spring Harbor, NY 11724, USA
[5]Present address: VERAXA Biotech GmbH, Carl-Friedrich-Gauß-Ring 5, 69124 Heidelberg, Germany
[6]Present address: Institut de Génétique Moléculaire de Montpellier, Université de Montpellier, CNRS, Montpellier, France
[7]Lead contact
*Correspondence: christoph.mueller@embl.de
https://doi.org/10.1016/j.celrep.2022.111316

SUMMARY

RNA polymerase (Pol) III is specialized to transcribe short, abundant RNAs, for which it terminates transcription on polythymine (dT) stretches on the non-template (NT) strand. When Pol III reaches the termination signal, it pauses and forms the pre-termination complex (PTC). Here, we report cryoelectron microscopy (cryo-EM) structures of the yeast Pol III PTC and complementary functional states at resolutions of 2.7–3.9 Å. Pol III recognizes the poly(dT) termination signal with subunit C128 that forms a hydrogen-bond network with the NT strand and, thereby, induces pausing. Mutating key interacting residues interferes with transcription termination *in vitro*, impairs yeast growth, and causes global termination defects *in vivo*, confirming our structural results. Additional cryo-EM analysis reveals that C53-C37, a Pol III subcomplex and key termination factor, participates indirectly in Pol III termination. We propose a mechanistic model of Pol III transcription termination and rationalize why Pol III, unlike Pol I and Pol II, terminates on poly(dT) signals.

INTRODUCTION

Eukaryotic RNA transcription is carried out by multiple DNA-dependent RNA polymerases (Pols). Pol I transcribes ribosomal RNA (rRNA). Pol II produces messenger RNAs (mRNAs) and various non-coding RNAs. Pol III synthesizes short, abundant RNA molecules such as transfer RNAs (tRNAs), the U6 small nuclear RNA (snRNA), and the 5S rRNA. Pol III is specialized to cope with the high demand of its target transcripts and, as such, requires fewer factors to initiate, elongate, and terminate transcription.

Pol III, similar to Pol I and Pol II, contains a 10-subunit core and a 2-subunit stalk domain. In addition, it features the C53-C37 heterodimer and the C82-C34-C31 heterotrimer. C53-C37 shares structural homology with the Pol II general transcription factor (GTF) TFIIF. Pol III also harbors subunit C11 (RPC10 in humans), whose C-terminal domain is homologous to the RNA-cleaving domain of the Pol II elongation factor TFIIS (Chedin et al., 1998). Similar to TFIIF and TFIIE, C53-C37 and C82-C34-C31 are required to initiate transcription (Brun et al., 1997; Kassavetis et al., 2010; Landrieux et al., 2006; Lefèvre et al., 2011; Thuillier et al., 1995; Wang and Roeder, 1997). C53-C37 and C11 are also crucial for Pol III transcription termination (Arimbasseri and Maraia, 2013, 2015; Chedin et al., 1998; Landrieux et al., 2006; Mishra and Maraia, 2019; Mishra et al., 2021; Rijal and Maraia, 2013).

Transcription termination is the final step in the transcription cycle and involves the release of DNA and RNA. As for Pol I and Pol II, a multitude of accessory factors are needed for transcription termination (Porrua and Libri, 2015; Richard and Manley, 2009). In contrast, Pol III relies on fewer elements to terminate transcription. Except for the helicase Sen1, which was recently reported to function in Pol III transcription termination (Rivosecchi et al., 2019; Xie et al., 2022) and likely acts as a "fail-safe" factor to help the release of Pol III molecules that fail to terminate in the first place (Xie et al., 2022), Pol III relies on only its built-in subunits and a termination sequence on the DNA to terminate transcription. The termination process allows fast recycling of Pol III to a new round of transcription in a process termed facilitated recycling (Dieci and Sentenac, 1996). Pol III terminates transcription on continuous stretches of thymine bases (dT) on the non-template (NT) strand of the DNA (Allison and Hall, 1985; Bogenhagen and Brown, 1981; Cozzarelli et al., 1983; Watson et al., 1984). Yeast Pol III requires at least 5 dTs to correctly terminate transcription (Allison and Hall, 1985) and, *in vitro*, does not rely on external factors to do so (Braglia

et al., 2005; Landrieux et al., 2006). Pol III uses its subunits C160 (Rijal and Maraia, 2016), C128 (James and Hall, 1990; Shaaban et al., 1995, 1996), C53-C37 (Arimbasseri and Maraia, 2013; Landrieux et al., 2006; Rijal and Maraia, 2013), and C11 (Chedin et al., 1998; Iben et al., 2011; Landrieux et al., 2006) to terminate transcription. C11 is also critical for the facilitated recycling process (Landrieux et al., 2006; Mishra et al., 2021). Prior to termination, Pol III slows down (Rijal and Maraia, 2016), to which C53-C37 contributes (Arimbasseri and Maraia, 2013). When Pol III encounters the poly(dT) termination sequence, it pauses on the 4th dT, thus forming the pre-termination complex (PTC), and C53-C37 was shown to be critical for PTC formation (Arimbasseri and Maraia, 2015). How Pol III recognizes the poly(dT) termination signal in the context of the Pol III PTC and how this facilitates pausing of Pol III and predisposes it for the termination process was, however, not known.

Structural insights into Pol III transcription could be obtained from initiating (Abascal-Palacios et al., 2018; Han et al., 2018; Vorländer et al., 2018) and elongating yeast Pol III (Hoffmann et al., 2015) via cryogenic electron microscopy (cryo-EM). In addition, structures of human Pol III were recently determined (Girbig et al., 2021; Li et al., 2021; Ramsay et al., 2020; Wang et al., 2021). A recent cryo-EM structure of the human Pol III PTC at 3.6 Å resolution showed that subunit RPC2 (the human ortholog to C128) recognizes the poly(dT) termination sequence (Hou et al., 2021). However, to what extent the contact sites between RPC2 and the termination sequence are critical to termination is still not known, due to a lack of functional validation of this interaction. Furthermore, the human Pol III PTC structure could not explain why C53-C37 (RPC4-RPC5 in humans) is critical for correct termination.

Here, we report the cryo-EM structure of the yeast Pol III PTC at a resolution of 2.8 Å. The structure confirms that C128 recognizes the poly(dT) termination signal and explains how pausing is achieved, which we extensively validate with structure-function studies. We also present complementary structures that shed light on how C53-C37 participates in transcription termination and how PTC formation may drive the subsequent termination process.

RESULTS

Purified yeast Pol III terminates transcription *in vitro*

To study the molecular mechanism of Pol III transcription termination on poly(dT) sequences, we first tested if the yeast Pol III sample used by us in earlier structural studies (Hoffmann et al., 2015; Vorländer et al., 2018, 2020) is also capable of terminating transcription on poly(dT) sequences. We used a double-stranded (ds) DNA construct composed of the *S. cerevisiae* U6 snDNA gene promoter and followed by the 3′ flanking sequence of the *S. cerevisiae* tRNA gene tL(CAA)L, which contains a strong 5-dT termination signal (Braglia et al., 2005) (Figure S1A). Recruitment of Pol III to the promoter DNA was facilitated by the addition of the Pol III GTF TFIIIB. A time course showed the appearance of a strong RNA band (visualized by supplementation with radioactively labeled UTP) at the expected size of ca. 35 nt, indicating that Pol III pauses and presumably terminates on the termination site (Figure S1B). Furthermore, Pol III paused or terminated on the 5-dT signal but not on the sequences carrying only 3 or 4 dTs (Figure S1C). Instead, termination readthrough (RT) products could be observed that corresponded to transcripts that were released once Pol III reached the end of the dsDNA. While this assay does not allow us to distinguish between pausing and termination, a similarly prepared batch of purified Pol III was recently shown to efficiently terminate on a 5-dT termination sequence on immobilized DNA templates (Xie et al., 2022). Together, these results confirm that Pol III is able to pause, and presumably terminate, on its own *in vitro* in a promoter-dependent transcription setup.

A 7-dT signal traps Pol III in a pre-termination state

To determine the structure of the Pol III PTC, we trapped Pol III in the PTC conformation by incubating it with a transcription scaffold that contained a 7-dT termination signal on the NT-DNA strand (Figure 1A). The scaffold also featured a 12-nt mismatch between the template (T) and the NT strand, thereby resembling an open transcription bubble. The DNA:RNA hybrid was also substituted so that it did not carry a poly(dA:rU) sequence to prevent spontaneous termination. We compared the capacity of Pol III to extend the RNA oligonucleotide in a 7-dT (PTC-like) or 2-dT (elongation complex [EC]-like) scaffold (Figure 1B). Addition of nucleoside triphosphates (NTPs) induced extension of the RNA primer on both scaffolds. However, on the EC scaffold, Pol III primarily transcribed long RNA products (lane 4), whereas a strong RNA band, just 3 bases downstream of the 3′ end of the RNA primer used was detected on the PTC scaffold (lane 8). The appearance of this RNA band, which could hardly be observed on the EC scaffold, indicated that Pol III pauses in the presence of the 7-dT signal on the NT strand and that the 7-dT scaffold traps Pol III in a PTC-like state.

Structure of the yeast Pol III PTC

Next, we assembled the yeast Pol III complex on the 7-dT PTC scaffold and acquired a high-resolution cryo-EM dataset (Data S1). Processing the data yielded a 3D reconstruction of the Pol III PTC with a nominal resolution of 2.8 Å that locally extended to 2.5 Å (Data S1). The cryo-EM map (map A in Data S1) showed a clear signal for the bound nucleic acids, with the downstream dsDNA and the DNA:RNA hybrid being well resolved (Figures 1C and S2A). The C160 bridge helix and trigger loop, which are both important active-site elements, are fully folded (Figure S2A). The C-terminal domain of C11, which was not resolved in the yeast Pol III EC structure, adopts an ‘‘outside funnel’’ conformation that is similar to that in apo yeast Pol III (Hoffmann et al., 2015) but differs from the ‘‘outside funnel’’ conformation in human Pol III (Girbig et al., 2021) (Figure S2B). Thanks to the improved quality of the 3D reconstruction of the Pol III PTC, we could extend the Pol III structural model compared with existing models. Additional densities near the heterodimer and in the heterotrimer could be assigned to C53 (aa 195–224) and C31 (aa 101–161), respectively (Figures S2C and S2D). We further assigned additional densities, one in the DNA binding cleft formed by subunit C160 and one near subunit AC40 (aa 311–329), to molecules of the detergent CHAPSO, which was used to optimize cryo-EM grid preparation (Figures S2E and S2F).

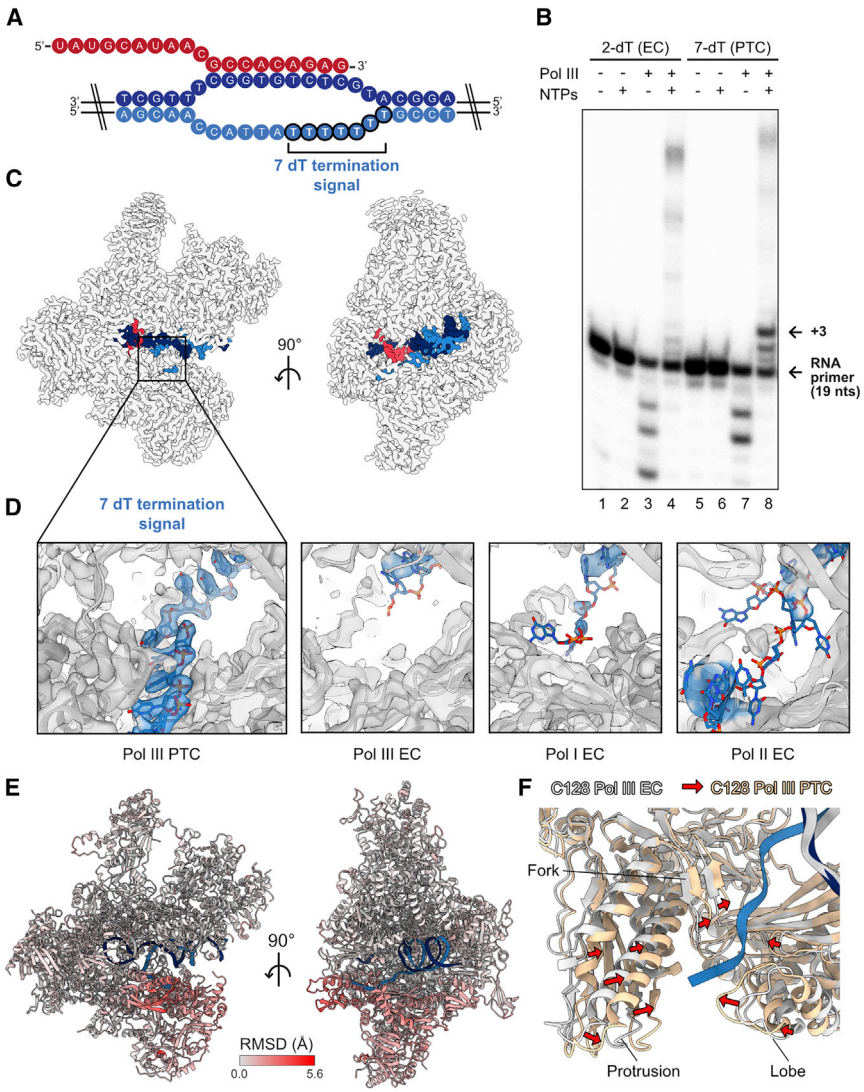

Figure 1. Yeast Pol III PTC structure

(A) Schematic of the 7-dT transcription scaffold. Red, RNA; dark blue, T strand; light blue, NT strand.

(B) RNA primer extension experiment. The elongation complex (EC) scaffold contains 2 dTs on the NT strand (left), and the PTC scaffold contains 7 dTs (right). Image contrast was adjusted for clarity.

(C) Cryo-EM reconstruction of the yeast Pol III PTC in two different views. Nucleic acids are colored as in (A).

(D) Close-up view onto the NT-strand binding region of Pol III PTC (this study), Pol III EC (this study), Pol I EC (EMDB: 0240; PDB: 6HLR), and Pol II EC (PDB: 5C4J; $2F_{obs} - F_{calc}$ calculated at 1.2 σ).

(E) Atomic model of the yeast Pol III PTC colored by root-mean-square deviation (RMSD) between the Pol III EC (not shown) and the Pol III PTC.

(F) Local contraction of subunit C128 around the NT strand upon PTC formation. Conformational changes from EC to PTC in subunit C128 are depicted as red arrows.

Importantly, the cryo-EM reconstruction showed a strong signal of the unpaired NT strand and allowed building of the complete 7-dT termination signal (Figure 1D). Because the cryo-EM sample preparation conditions differed between the Pol III PTC and the earlier reported Pol III EC (Hoffmann et al., 2015), we determined a Pol III EC structure under exactly the same conditions as for the Pol III PTC and only reduced the number of the dTs on the NT strand. Cryo-EM data collection and processing yielded a 3D reconstruction of the Pol III EC control (map B) with a nominal resolution of 3.4 Å that locally reached 2.9 Å (Data S2). While the cryo-EM signals of unrelated polypeptide elements were of comparable qualities, the NT strand was only poorly resolved in the Pol III EC (Figure 1D). We further compared our cryo-EM reconstruction with reported structures of other eukaryotic RNA Pols. The comparison revealed that the NT strand in the Pol III PTC is also much better resolved than the NT strand in the yeast Pol I EC (Tafur et al., 2016) and yeast Pol II EC structures (Barnes et al., 2015) (Figure 1D). Hence, the strong signal of the NT strand is a specific feature of the Pol III PTC and indicates that Pol III is capable of recognizing the poly(dT) termination signal in a specific manner.

Superimposition with the Pol III EC shed light on conformational changes upon recognition of the termination signal as shown by a local contraction of subunit C128 around the NT strand (Figures 1E and 1F). The contracting regions of C128 can be mapped to the C128 lobe (aa 196–370), protrusion (aa 60–195 and 371–439), and fork (aa 440–521) domains. In addition, the C53-C37 heterodimer, which binds the C128 protrusion domain, subunit C11, and the jaw domain of C160 contract toward the direction where the NT strand resides. Compared with the yeast Pol I and Pol II EC structures, the conformations of the Pol III fork (see below) and lobe domains differ considerably in size and conformation (Figures S3A and S3B). The Pol I lobe would clash with the modeled NT strand of the superimposed Pol III PTC (Figure S3A), indicating that the NT strand follows a different path in Pol I. The Rpb2 lobe region near the NT strand was not modeled in the only yeast Pol II EC structure that features a fully built transcription bubble (Barnes et al., 2015), presumably because it was too flexible (Figure S3B). Consequently, the path of the NT strand and its exit regions differ between Pol I, Pol II, and Pol III (Figure S3C). The NT strand in the Pol III PTC runs along a narrow cavity, which does not form in Pol I and Pol II. These structural differences suggest that the NT strand is more tightly bound in Pol III (when a poly[dT] termination signal is present) than it is in Pol I and Pol II, which would rationalize why only Pol III canonically terminates on poly(dT) signals.

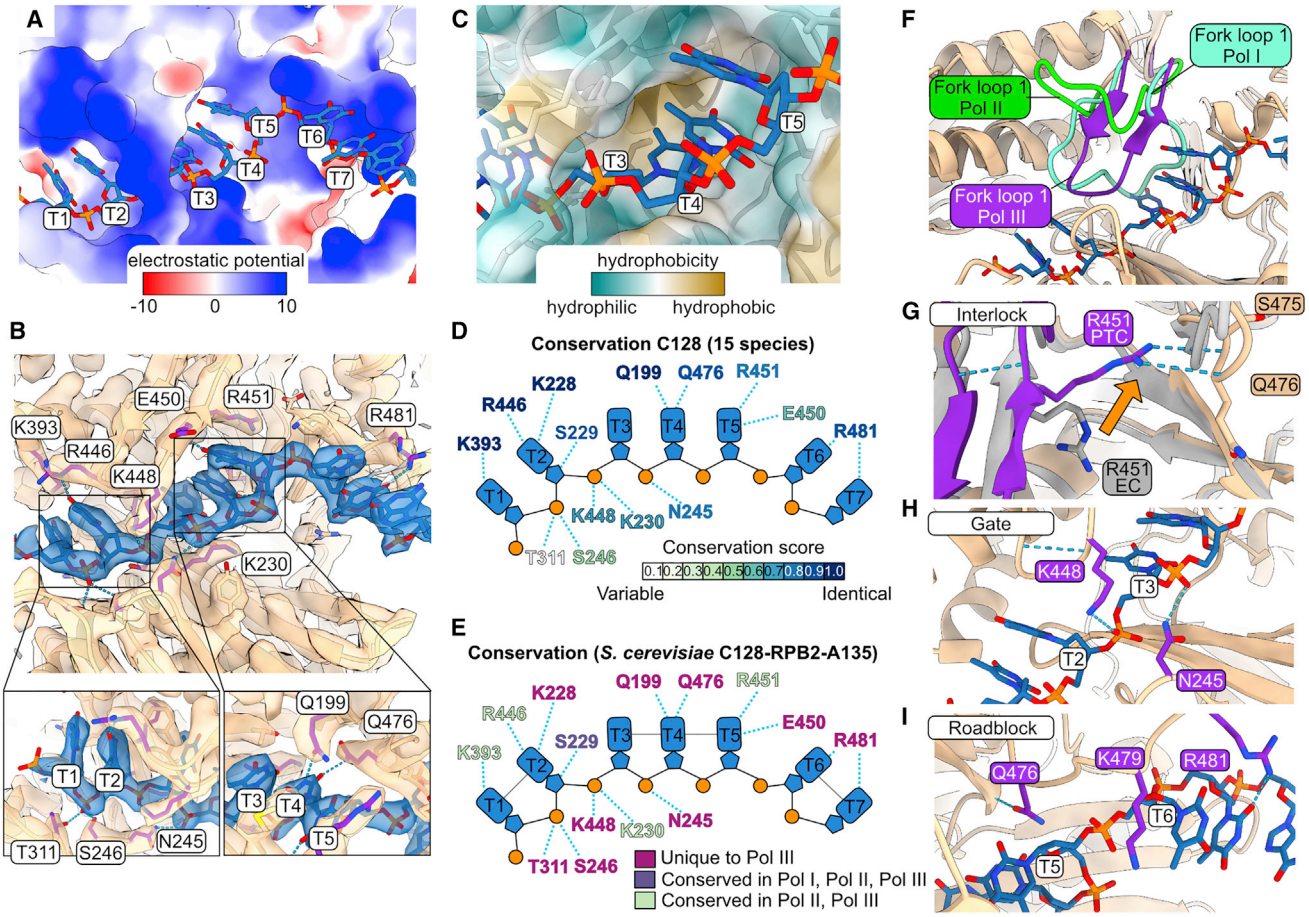

Figure 2. Termination signal recognition in the Pol III PTC

(A) Surface representation of C128, colored by electrostatic potential in kcal/(mol·e) at 298 K (red, negative; blue, positive).

(B) Hydrogen bonds between the 7-dT termination sequence (colored in blue) and C128 (colored in wheat). Residues that form H bonds (blue dashed lines) with the NT strand are depicted as purple sticks. Cryo-EM densities are shown as transparent surfaces.

(C) A hydrophobic groove formed by fork loop 1 accommodates the methyl groups of dT_3 and dT_4. C128 is shown in the ribbon mode with its surface presentation transparent and colored by hydrophobicity.

(D) Nucleotide plot of the C128-NT-strand interaction. Residues are colored according to conservation scores (see STAR Methods). H bonds, blue dashed lines. See Data S5 for the corresponding multiple sequence alignment.

(E) Conservation between H-bond-contacting residues in C128 and *S. cerevisiae* paralogs A135 (Pol I) and Rpb2 (Pol II). See Data S6 for the corresponding multiple sequence alignment.

(F) Fork loop 1 folds differently between Pols I, II, and III. The fork loops 1 of C128 (Pol III PTC, this study), A135 (Pol I EC; PDB: 6HLR), and Rpb2 (Pol II EC; PDB: 5C4J) are shown.

(G) C128 residue R451 functions as an interlock. The fork loops in the Pol III PTC and EC are colored in purple and gray, respectively. Conformation changes are indicated by an orange arrow.

(H) C128 residue K448 forms, together with N245, a molecular gate that guides the NT strand and breaks base stacking between dT_2 and dT_3.

(I) C128 residue K479 defines the path of the NT strand and disrupts base stacking between dT_5 and dT_6, thereby functioning as a molecular roadblock.

Subunit C128 specifically recognizes the termination signal

In the Pol III PTC structure, the NT strand is exclusively bound by subunit C128 and is embedded into a positively charged groove (Figure 2A). C128 forms 14 hydrogen bonds (H bonds) with the phosphate backbone and the bases of the 7 dTs (Figure 2B). The residues that bind the NT strand all reside in the lobe, protrusion, and fork domains that contract upon recognition of the termination signal (Figures 1E and 1F). In addition, the methyl groups of dT_3 and dT_4 are embedded into a hydrophobic cavity formed by the fork loop (FL) 1 element (aa 440–453), thereby allowing Pol III to distinguish between a thymine and a cytosine base (Figure 2C).

Next, we analyzed to what extent the residues that bind the NT strand are conserved among C128 orthologs from various eukaryotes (see STAR Methods) (Figure 2D). Four amino acids (Q199, K228, K393, and R446) are identical in all analyzed supergroups, and five amino acids have a high conservation score of 0.8–0.9 (S229, N245, R451, Q476, and R481). Another four residues (K230, S246, K448, and E450) exhibit moderate

conservation scores of 0.5–0.7, and only one residue (T311) is not conserved across the analyzed species. We also asked to what extent these residues are conserved across *S. cerevisiae* C128 and its two paralogs in Pol I (A135) and Pol II (Rpb2). The residue conservation analysis between the three paralogs revealed that 9 of the 14 residues (Q199, K228, N245, S246, T311, K448, E450, Q476, and R481) are unique to Pol III (Figure 2E). Hence, C128 utilizes a set of conserved residues that are mostly unique to Pol III to engage tightly with the poly(dT) termination signal.

Multiple key residues that contribute to NT-strand recognition can be mapped to the FL 1 and FL 2 (aa 475–486) elements of subunit C128, which clearly folds differently in Pol III, comparing this region with the equivalent one in Pol I and Pol II (Figure 2F). The FL 1 elements of Pol I (aa 469–483) and of Pol II (aa 466–478) adopt loop-like folds, whereas the Pol III FL 1 folds into a β hairpin, and its tip points into a different conformation compared with Pol II. This conformation is required to form the hydrophobic cavity of C128 and positions four residues (R446, K448, E450, and R451) so that they can bind the NT strand.

Superimposing the Pol III PTC and EC structures revealed that residue R451 in FL 1 changes its conformation upon PTC formation and flips by ca. 90° and forms two H bonds with the peptide backbone of FL 2, thereby functioning as an interlock that keeps FL 1 in a fixed position (Figure 2G). Another important residue is K448, which forms a molecular gate with N245 and, thereby, guides the NT strand and disrupts the base stacking between dT_2 and dT_3 (Figure 2H). FL 2 bears three key residues for NT-strand coordination: Q476 forms an H bond with the dT_4 base, R481 forms two H bonds with dT_6 and dT_7, respectively, and K479 functions as a positively charged molecular roadblock that interrupts the base stacking between dT_5 and dT_6 (Figure 2I) and guides the NT strand to follow its defined path.

In summary, we interpret the tight H-bond network and the embedment of the methyl groups of the dT_3 and dT_4 bases as physicochemical barriers that counteract the translocation of Pol III along the DNA. Pol III uses a unique set of conserved residues, not only to form these physicochemical barriers but also to define the path of the NT strand, which explains how termination signal recognition and pausing prior to termination is achieved.

Mutating key dT-interacting residues in C128 interferes with transcription termination *in vitro*

To confirm the physiological relevance of our structural analysis of the Pol III PTC, we performed complementary functional experiments. We used CRISPR-Cas9 genome engineering of yeast cells to introduce several single-residue point mutations into C128: Q199R, K448A, R451V, R481G, and H225L. We also generated a C128 mutant that harbored three substitutions in FL 2: Q476A, K479A, and R481G (hereinafter referred to as the triple mutant). Q199 forms an H bond with dT_4, is unique to Pol III, and is conserved in all analyzed eukaryotic species. K448 forms the molecular gate, R451 functions as the interlock, and R481 forms two H bonds with dT_5 and dT_6. H225 was chosen because it sits in the lobe region of C128 and forms a potential H bond with D72 residing in a helix that contracts upon PTC formation. The triple mutant contains substitutions in two H-bond-forming residues (Q476 and R481) and in K479, which acts as the molecular roadblock. In all residues, except one (Q476), we were guided by the multiple-sequence alignment of Pol subunits C128, Rpb2, and A135 to replace the C128 residues with their counterparts in Rpb2 (Pol II-like) or A135 (Pol I-like).

We purified wild-type (WT) and mutant Pol III variants to homogeneity (Figure 3A) and tested the effects of the C128 mutants using an *in vitro* transcription assay with a tailed template containing a single-stranded overhang on the T strand (Figure 3B). The constructs contained either a 6-dT termination signal or a 3-dT signal through which Pol III should be able to transcribe without terminating. We designed the construct to contain the first guanine base (dG) on the NT strand downstream of the termination sequence so that Pol III RT products could be captured by using only CTP, ATP, and UTP in the transcription reaction. As expected, WT Pol III paused or terminated efficiently on the 6-dT termination signal as shown by a robust signal at the position where the termination signal sits (Figure 3C, lane 2). The 3-dT reaction, in contrast, did not show any sign of termination and, instead, RT products accumulated at the first dG (lane 11). Unexpectedly, we also observed additional RT bands downstream of the first dG. This could be due to misincorporation of nucleotides (as reported to be possible *in vitro* in both Pol II (Thomas et al., 1998) and Pol III (Alic et al., 2007) transcription systems) or a potential GTP contamination in the transcription reaction mix, which, in our point of view, does not affect the conclusions drawn below. Notably, termination products are not as pronounced in our tailed-template experiments compared with our promoter-dependent transcription assays (Figure S1B), because Pol III can undergo facilitated recycling in the promoter-dependent transcription setup, which is not expected to occur in the tailed-template setup.

Strikingly, we observed a strong reduction of the pausing or termination efficiency for all mutants, except for H225L (Figure 3C, lanes 3–8, and Figure 3D). We observed the strongest reduction in pausing/termination efficiency for the Q199R mutant (ca. 4-fold), followed by the triple and R451V mutants (both ca. 3-fold). The K448A and R481G mutants showed a more modest, but still clear, reduction (ca. 1.7-fold). For the Q199R and R451V mutants, we also noticed an increase in RT products (Figure 3C, lanes 4 and 5). The tested mutants did not show any significant changes in the production of RT transcripts on the 3-dT control construct. Hence, the tested Pol III mutations affected only Pol III pausing or termination on the poly(dT) sequence but not transcription per se. Because we introduced the mutations to interfere with the recognition of the poly(dT) signal, which serves as a pausing signal, it is likely that the observed effects reflect pausing defects. It is noteworthy that transcription pausing and termination are tightly coupled, as pausing is a requirement for Pol III termination to take place (Arimbasseri and Maraia, 2013, 2015; Rijal and Maraia, 2016). Accordingly, any mutations that interfere with Pol III pausing will, most likely, also impair termination. The tailed-template transcription assay, thus, confirmed the importance of the amino acids Q199 (H bond with dT_4), R451 (interlocks FL 1), Q476 (H bond with dT_4), K479 (molecular roadblock), and R481 (H bonds with dT_6 and dT_7). It also showed that the K448 molecular gate functions in transcription termination, but it seems less important than the other tested residues

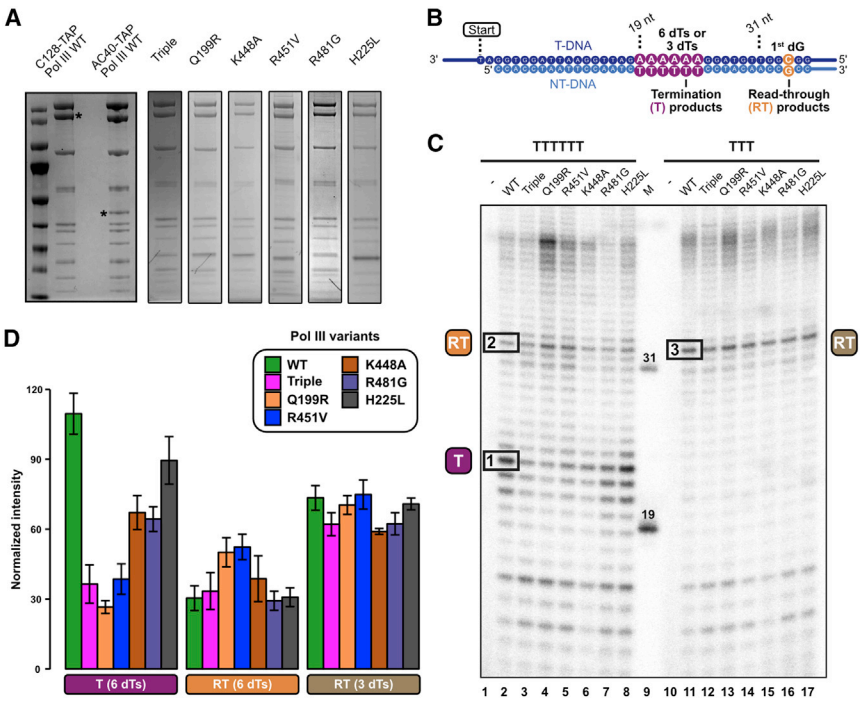

Figure 3. Mutating Pol III C128 on specific sites interferes with Pol III termination *in vitro*

(A) Protein gels of purified *S. cerevisiae* Pol III WT and mutant samples. Asterisks mark the tagged subunits in the C128-TAP (used for the experiments) and AC40-TAP (loaded as control) Pol III samples. Individual protein lanes are cropped from protein gels prepared after each purification.

(B) Schematic of the tailed-template DNA construct. The positions of the poly(dT) termination signal and of the first guanine base (dG) are highlighted.

(C) *In vitro* transcription experiment on tailed-template DNA constructs. Experiments on WT and mutant Pol III variants were done on either a 6-dT or a 3-dT construct. The denaturing RNA gel corresponds to one of three independent experiments. RNA bands used to quantify the Pol III transcription products are indicated by black boxes for the Pol III WT lanes. T, termination; RT, readthrough. Gel boundaries (top, bottom) were cropped and image contrast was adjusted for clarity.

(D) Quantification of the Pol III transcription products indicated in (C). Bar plots represent normalized RNA band intensities (mean ± SD) from three technical replicates. For lane 15 (K448A), two technical replicates were used.

as its substitution showed a less severe pausing/termination deficiency.

Pol III C128 mutations affect yeast viability and cause global termination defects *in vivo*

We next asked whether the C128 mutations also affect Pol III function *in vivo* and first compared the growth of the WT and the different C128 mutant strains (Figure 4A). For the triple mutation, we observed a severe thermosensitive growth phenotype at 37°C, whereas growth was unaffected at 30°C or 25°C. We could also observe a slight thermosensitive phenotype for the R481G mutant. The Q199R displayed a clear growth defect at 30°C, which was even more pronounced at 25°C. These results support the idea that these mutations compromise Pol III function *in vivo*. For the K448A and R451V mutants, we did not observe any growth phenotype, suggesting that the effect of these mutations on Pol III activity is not severe enough to impair yeast growth.

We then directly assessed whether the most disruptive C128 mutations provoke Pol III termination defects *in vivo*. To this end, we generated high-resolution genome-wide maps of transcribing Pol III by UV cross-linking and analysis of cDNAs (CRAC), which allows mapping the position of Pol III with nucleotide resolution (Candelli et al., 2018; Granneman et al., 2009). We performed these experiments in strains carrying the WT, Q199R, R451V, or triple mutant version of C128 (Figures 4 and S4) grown at permissive temperature (i.e., 30°C). We obtained very specific and reproducible Pol III signals in the two biological replicates, with most of the reads mapping to Pol III-transcribed genes (i.e., tRNA, 5S RNA, and a few additional genes; Figure S4). Metagene analysis of Pol III distribution around tRNA genes (Figure 4B) indicates that a considerable fraction of WT Pol IIIs read through the primary terminator (i.e., the first T track after the 3′ end of the gene), in agreement with previous studies (Turowski et al., 2016; Xie et al., 2022). Importantly, we observed a significant increase in Pol III signal downstream of the primary terminator in the three mutants, indicating global transcription termination defects (Figure 4B and individual examples in Figure 4C). Clear termination defects were also observed at other Pol III-dependent genes such as the 5S and the *SNR52* genes (Figure S4E). Heatmap analysis of Pol III occupancy (log2 ratio) in each mutant relative to the WT showed that such an increase in the Pol III RT signal can be detected for the vast majority of tRNA genes (Figure 4D), further confirming the generality of termination defects. Among these mutants, Q199R exhibited the most pronounced termination defects. While the R451V mutant did not show a growth phenotype, it was defective in Pol III transcription termination, similar to the triple mutant or even to a slightly higher degree for some genes. The extent of transcription termination defects of the R451V and the triple mutant might not be high enough to induce growth defects at 30°C. Yet, at 37°C, growth might be more affected in the triple mutant because its residues form (when not mutated) several H bonds with the NT-strand bases, whereas R451 does not. Hence, altering the different modes of NT-strand recognition appears to affect yeast viability in different ways, suggesting that the formation of a tight H-bond network is the prime mode of NT-strand recognition.

To perform a more quantitative assessment of termination defects caused by the different C128 mutations, we computed for each tRNA gene the RT index (determined by the ratio of Pol III signals within 500 bp downstream of the primary terminator

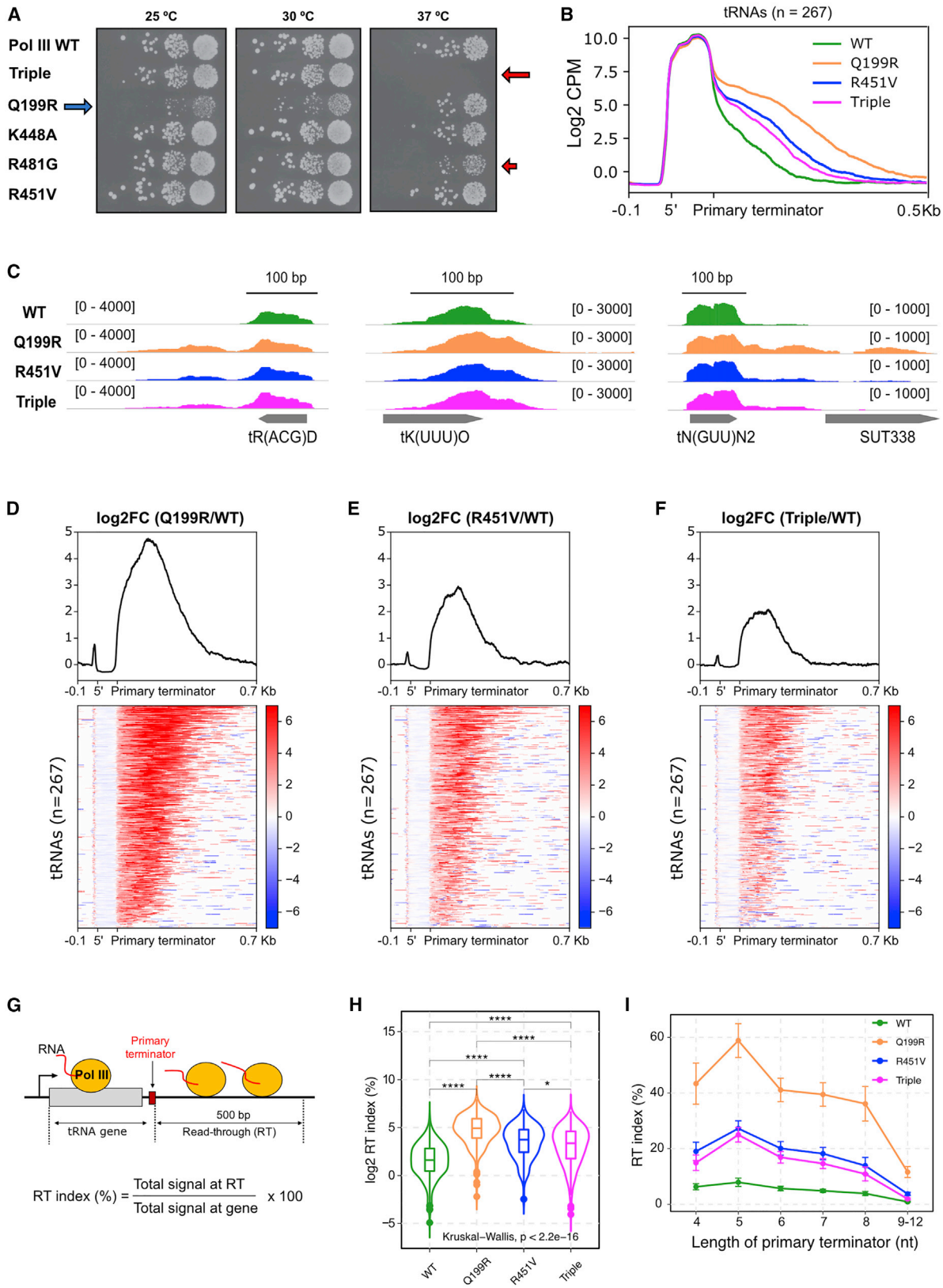

(legend on next page)

relative to the gene body, Figure 4G) in the WT and mutant strains. We observed an increase in the average RT index, and thus a decrease in the Pol III termination efficiency, in all mutants compared with the WT, with the largest increase in Q199R and a more moderate and similar increase in R451V and the triple mutant (Figure 4H). We considered the possibility that the different C128 mutations could have different impacts on the individual tRNA genes depending on the length of their terminator sequence. For instance, the Q199R mutation, predicted to prevent the interaction with the fourth T of the terminator, might not strongly affect termination at very long T tracks. To address this possibility, we analyzed the RT index on tRNA genes grouped according to the length of their primary terminator. However, we observed a similar behavior in the three mutants, namely a general increase in the RT index at all gene sets that tended to decrease as the length of the primary terminator increased (Figure 4I). Therefore, the introduced mutations reduce the efficiency of termination independent of the T-track length.

Altogether, these results indicate that mutations in C128 designed to interfere with the recognition of or the response to the poly(dT) termination signal impair Pol III transcription termination *in vivo*.

Structure of Pol III Δ sheds light on the role of C53-C37 in Pol III transcription termination

The structure of the Pol III PTC revealed a key role for C128 in Pol III transcription termination. However, it did not explain the function of C53-C37, which has been demonstrated to be essential for Pol III transcription termination but does not contact the NT strand directly in the Pol III PTC. To better understand the role of C53-C37, we determined the structure of a Pol III variant lacking C53-C37 and C11 (hereafter referred to as Pol III Δ). We purified Pol III Δ from an *S. cerevisiae* strain in which the C11 gene was substituted with its *S. pombe* ortholog, thereby causing loss of C53-C37 and C11 during protein purification (Kassavetis et al., 2010) (Figure 5A). We assembled Pol III Δ on the 7-dT PTC scaffold, subjected it to cryo-EM analysis, and obtained a 3.9 Å cryo-EM map (Data S3). Despite the lower resolution, the cryo-EM map was still of sufficient quality to build the Pol III Δ structure for comparison with the Pol III PTC. The Pol III Δ structure lacked the density for C53-C37 and C11 but clearly featured cryo-EM density for the bound DNA and RNA elements (Figure 5B). The cryo-EM signal corresponding to the NT strand was, however, much poorer than in the Pol III PTC, despite the presence of the 7-dT termination signal (Figure 5B). We further noticed that the fork, protrusion, and lobe elements of C128 adopted a relaxed, instead of a contracted, conformation (Figures 5B and 5C). Hence, the earlier described contraction of the Pol III core upon NT-strand recognition was essentially reversed in the absence of C53-C37 and C11. Instead, the conformation of the Pol III Δ core resembled that of the Pol III EC despite the presence of the termination signal (Figure 5D). We concluded from this observation that the C53-C37 heterodimer—although it does not directly contact the NT strand—indirectly assists Pol III termination by binding the lobe of C128 and positioning it for interaction with the NT strand.

NTP addition leads to a register offset between the unwound DNA strands

Finally, we set out to determine the structure of the Pol III PTC in the presence of NTPs. We incubated Pol III with the 7-dT PTC scaffold and with an NTP mix containing CTP, ATP, and UTP and obtained a 3D reconstruction (map D) of the Pol III PTC + NTPs (Figure 6A) at a nominal resolution of 2.7 Å (Data S4). We noticed that the upstream DNA was slightly better resolved, which encouraged us to perform masked 3D classification on the nucleic acid elements (Data S4). We, thereby, obtained a 3D map (map E) with a significantly improved signal of the upstream DNA moiety that allows the visualization of the complete transcription bubble (Figure 6B).

The cryo-EM densities in the Pol III PTC and PTC + NTPs structures were of sufficient quality to define the registers of the DNA:RNA hybrids (Figures 6C and 6D). In the Pol III PTC, the 3′-end guanine (G19) of the RNA oligonucleotide used sits on position i − 1, whereas the nucleotide addition side (i + 1) position is not occupied (Figure 6C). In the Pol III PTC + NTPs structure, the RNA was extended by at least 1 nt, and the bases of the hybrid were shifted by one position away from the nucleotide addition site, which was occupied by a newly attached cytosine (Figure 6D). We also observed a weak density that occupied position i + 1 and extended the RNA model with another adenosine (A21). Surprisingly though, we did not observe a register shift on the NT strand (Figures 6D and 6E), which was also very well resolved in the Pol III PTC + NTPs structure. Hence, the addition

Figure 4. Characterization of the effects of C128 mutations on cell growth and Pol III transcription termination *in vivo*

(A) Serial dilution analysis of the growth of C128 mutant strains at various temperatures. One of three technical replicates is shown. Red and blue arrows highlight heat- and cold-sensitive growth phenotypes, respectively.

(B) Metagene analysis of the Pol III distribution around tRNA genes. The signal covering the region between the 5′ end and the primary terminator (i.e., the first T track after the 3′ end of the mature tRNA) is scaled to 100 bp. Values on the y axis correspond to the mean coverage expressed as counts per million (CPM). Data are represented in the logarithmic scale. Two technical replicates were performed.

(C) Integrative Genomics Viewer (IGV) screenshots of examples of tRNA genes displaying termination defects in the indicated strains. Values within brackets correspond to the scale of the Pol III signal expressed in CPM. Only the signal on the strand hosting the tRNA gene is indicated.

(D–F) Heatmap analyses representing the log2 fold change (FC) of the Pol III signal in the indicated mutants relative to the WT at tRNA genes. The summary plots on the top were calculated using the average values for each position. tRNA genes in the heatmaps are sorted in the same order determined by the ranking of signals in (D).

(G) Scheme of a tRNA transcription unit indicating the gene body and the readthrough (RT) region.

(H) Comparison of the average RT index for tRNA genes in the indicated strains. "p" corresponds to the p value for the global comparison of the four groups according to the Kruskal-Wallis test. Asterisks denote the p values of pairwise comparisons (*$p \leq 0.05$; ****$p \leq 0.0001$).

(I) RT index of tRNA genes grouped according to the T-track length of their primary terminator in the indicated strains. Data points correspond to the average value, whereas error bars denote the standard error.

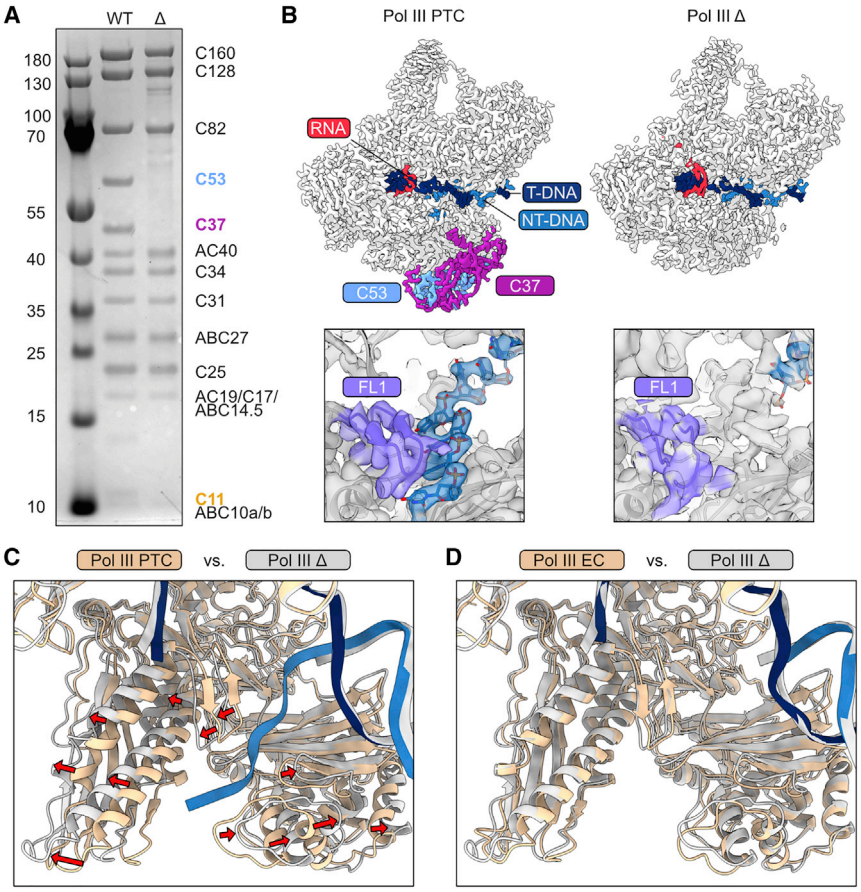

Figure 5. Cryo-EM structure of Pol III Δ

(A) Protein gel of Pol III WT and Pol III Δ. Figure modified from Xie et al. (2022) © the authors, some rights reserved; exclusive licensee AAAS. Distributed under a CC BY-NC 4.0 license (http://creativecommons.org/licenses/by-nc/4.0/).

(B) Top: comparison between the cryo-EM maps of the Pol III PTC (left) and Pol III Δ (right). The Pol III Δ map lacks C53-C37 and C11. Bottom: the NT-strand binding region in the Pol III PTC. Cryo-EM densities are shown as transparent surfaces.

(C) Superimposition of the Pol III and Δ Pol III PTC structures. Conformational changes are indicated by red arrows.

(D) Superimposition of the Pol III and Δ Pol III EC structures.

of NTPs induced a register shift of the DNA:RNA hybrid but left the NT strand unchanged.

DISCUSSION

Model of Pol III transcription termination

We determined the high-resolution cryo-EM structure of the yeast Pol III PTC at a resolution of 2.8 Å. Using genetic, biochemical, and high-resolution genomic approaches, we validated the conclusions of our structural analyses *in vitro* and *in vivo*. We also determined complementary structures of the Pol III Δ and the Pol III PTC in the presence of NTPs. Based on these insights, we propose a mechanistic model for Pol III transcription termination (Figure 7).

Pol III initiates transcription with the help of GTFs (step 1). When Pol III enters the elongation phase, the NT strand only loosely associates with Pol III. Once Pol III reaches a termination site that harbors at least 4 dT bases, C128 recognizes the termination signal, Pol III pauses, and the Pol III PTC forms (step 2). PTC formation is driven by the H-bond network between C128 and the termination sequence. The NT strand becomes ordered, and Pol III contracts around it. FL 1 establishes multiple H bonds with the NT strand and forms a hydrophobic cavity that accommodates the methyl groups of 2 dT bases. C128-mediated recognition of the termination signal is aided by C53-C37, which binds the C128 lobe domain. We earlier hypothesized that a flexible loop in C37 (aa 197–224), which connects two helices that bind the C128 lobe domain, participates in Pol III transcription termination by directly binding the NT strand (Hoffmann et al., 2015). Given that we did not observe such an interaction in the Pol III PTC, we need to revise this hypothesis and, instead, propose that binding of C53-C37 reduces the flexibility of C128 and, thereby, reinforces its tight interaction with the NT strand when the poly(dT) sequence is exposed. In the absence of C53-C37, Pol III would not be slowed down once it has reached the termination signal, thus preventing correct termination. This mode of function rationalizes the role of C53-C37 in transcription termination, which was, so far, poorly understood on a molecular level.

The interaction between the NT strand and C128 induces pausing, but Pol III still appears to be able to extend the RNA molecule, which "pulls" the T strand towards the active site (step 3). The strong interaction with the termination sequence hinders further translocation along the DNA and induces a register offset between the T and the NT strand. Such offset could trap Pol III in an unproductive state that might be sensed by subunit C11 (step 4). C11 is homologous to TFIIS, which is needed in the Pol II system to reactivate stalled Pol II by cleaving off backtracked RNA (Cheung and Cramer, 2011). We, therefore, speculate that C11 also senses an unproductive state of Pol III.

In attempts to rescue the stalled Pol III PTC, C11 may insert its catalytic C-terminal domain into the Pol III funnel. Insertion of C11 into the Pol III funnel has been recently shown to be concomitant with partial opening of the Pol III clamp domain that contacts the downstream DNA (Girbig et al., 2021) (step 5). However, transcription termination does not dependent on the RNA-cleavage activity of C11 (Landrieux et al., 2006; Mishra and Maraia, 2019; Mishra et al., 2021). We, therefore, propose that C11 insertion into the Pol III funnel serves as a destabilizing signal by opening the clamp domain so that Pol III loses its "grip"

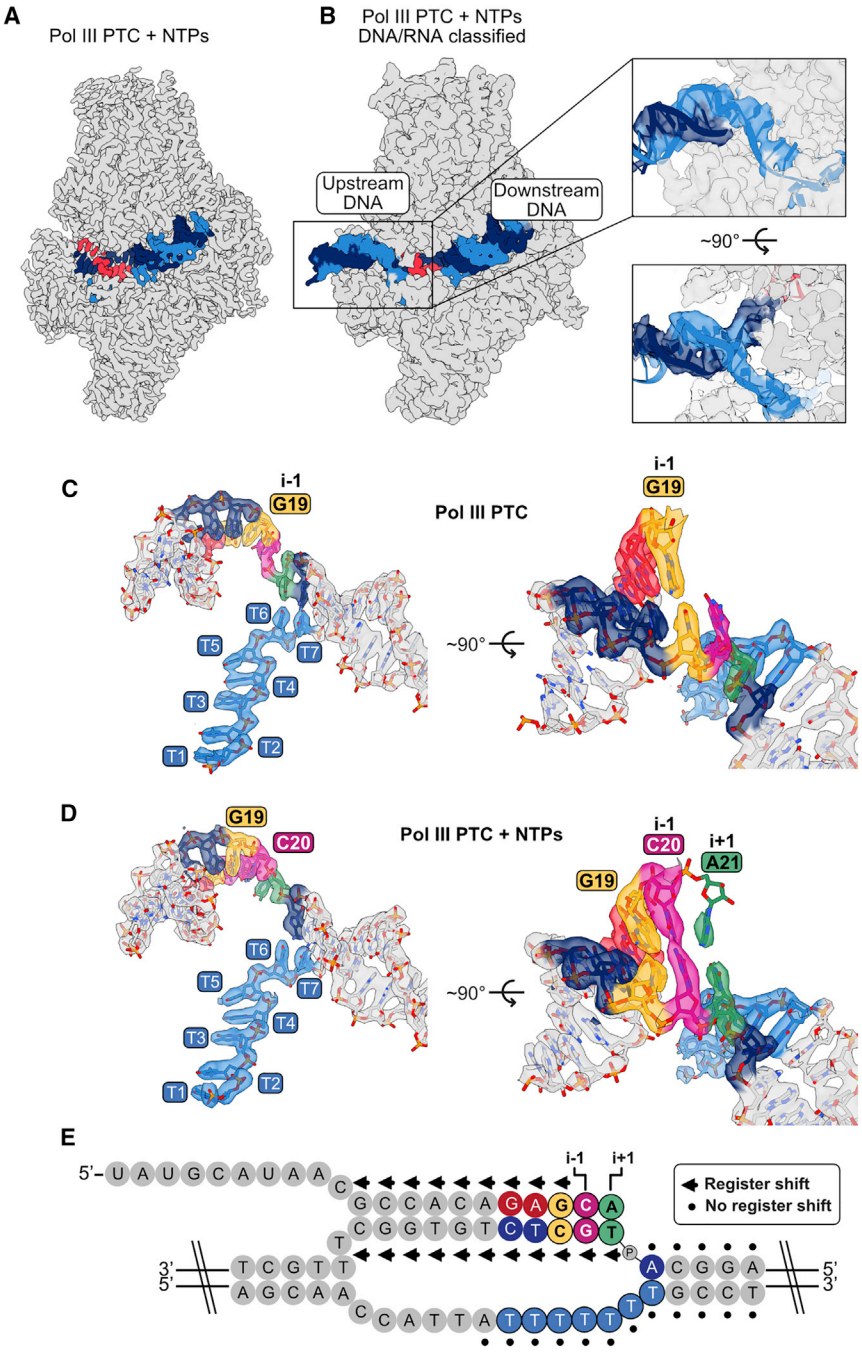

Figure 6. Structure of the Pol III PTC + NTPs

(A) Cryo-EM map of Pol III PTC + NTPs. Dark blue, T DNA; light blue, NT DNA; red, RNA.

(B) Improved signal for the upstream DNA, derived via masked classification on nucleic acid elements. A putative nucleic acid strand model for the upstream DNA is shown for illustrative purposes but was not included into the final Pol III PTC + NTPs model.

(C) Transcription bubble in the Pol III PTC. Nucleotides of interest are colored to illustrate the register of the DNA:RNA hybrid and of the NT strand.

(D) Transcription bubble in the Pol III PTC + NTPs structure. Nucleotides are colored as in (C). The nucleotide addition site (i + 1) shows weak density (green) for another added nucleotide.

(E) Schematic of the poly(dT) transcription bubble highlighting the observed register shift (arrows) in the DNA:RNA hybrid but not on the NT strand (dots) upon addition of NTPs.

on the downstream DNA. Owing to the poly(dT) termination signal on the NT strand, a dA:rU hybrid forms in the active site, which is much less stable than hybrids with other sequences (Martin and Tinoco, 1980) (step 6). The funnel insertion of C11 could reinforce dismantling of the already unstable hybrid. Since the DNA:RNA hybrid itself is an important stabilizing element of the Pol III EC, the falling apart of the hybrid would consequently cause the Pol III PTC to collapse and to release both the DNA and the nascent RNA molecule (step 7).

C11 is also required for facilitated recycling of Pol III (Dieci and Sentenac, 1996; Landrieux et al., 2006). This mode of function could be assigned to the linker domain that links the N-terminal and the C-terminal domain (CTD) of C11 (Mishra et al., 2021). We speculate that terminated Pol III still harbors the C11 CTD inserted into its funnel and as an increased propensity to reinitiate transcription (step 8). The cryo-EM structures of the yeast Pol III initiation complexes revealed that the clamp adopts a closed conformation in the Pol III PIC (Abascal-Palacios et al., 2018; Vorländer et al., 2018) and, thus, needs to first open up to allow recruitment of Pol III to the promoter DNA. We propose that this process could be assisted by the insertion of C11 into the funnel.

Comparison between the yeast and the human Pol III PTC

When this article was in preparation, the structure of the human Pol III PTC at a resolution of 3.6 Å was reported (Hou et al., 2021). The human Pol III PTC showed characteristics comparable to those of the yeast PTC (Figures S5A and S5B), except that the DNA:RNA hybrid is more poorly resolved in the human Pol III PTC (Figures S5C and S5D). The 6 bases of the poly(dT) termination signal, however, were equally well resolved, and multiple H bonds formed between the termination signal and RPC2 (the human C128 ortholog). The NT strand follows a similar path and is contacted by the FL 1 and FL 2 (Figures S5E and S5F). The lobe, protrusion, and fork elements also contract around the NT strand. Together with our biochemical investigation of the key residues in C128, our investigation of

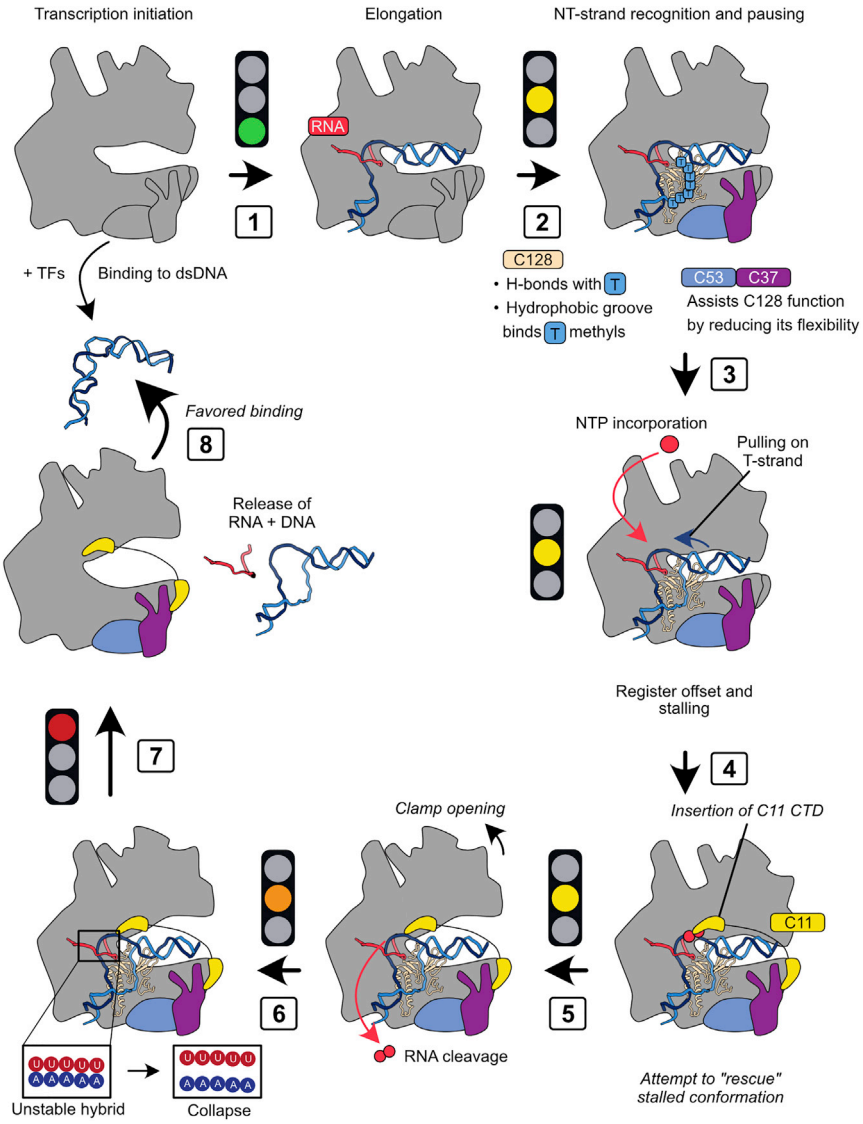

Figure 7. Model of Pol III transcription termination

The model combines the structural and biochemical data presented here with literature-based hypotheses (italicized).

complementary structures, and the *in vivo* validation of its physiological relevance, the two Pol III PTC structures, thus, support and complement each other.

Notably, the number of dTs that are required for Pol III transcription termination differs between human and yeast. Whereas *S. cerevisiae* Pol III needs at least 5 dTs to terminate, the majority of human tRNA genes possess only a 4-dT termination site (Braglia et al., 2005), which is why human Pol III must be more sensitive to shorter dT-tracks. Given that the human and yeast Pol III PTCs recognize the NT strand in similar manners, we speculate that the differences between the two species are due to a less stably bound DNA:RNA hybrid in the active site, or to differences in the contribution of the C11 subunit (RPC10 in humans) to termination. Indeed, we noticed that the DNA:RNA hybrid in the human Pol III PTC was less well resolved than in the yeast Pol III PTC (Figures S5A–S5D). However, we could not observe any obvious differences in the amino acids that contact the DNA:RNA hybrids in the two structures that might account for the observed differences, suggesting that the observed differences pertain to the impact of C11/RPC10. In both PTC structures, the CTDs of C11/RPC10 are positioned outside of the Pol III funnel. Human RPC10 is able to dynamically monitor the active site of Pol III because it adopts either an "outside funnel" (Girbig et al., 2021) or an "inside funnel" conformation (Girbig et al., 2021; Li et al., 2021; Wang et al., 2021). A similar conformation has not yet been captured for yeast Pol III, indicating that human RPC10 has a higher tendency to enter the Pol III active site. We hypothesize that the active site of human Pol III is, owing to the action of human RPC10, more sensitive to unstable poly(-dA:rU) hybrids than yeast Pol III, which could explain why human Pol III terminates transcription on fewer dTs.

Limitations of the study

Our structural analysis reveals how Pol III recognizes and pauses on poly(dT) termination signals. Although we provide a possible model of the full Pol III termination process, it remains speculative until the precise role of the RNA-cleaving subunit C11 is deciphered, which will require additional structural and biochemical analysis. The Pol III PTC sample also did not contain a poly(dA:rU) hybrid to prevent premature transcription termination. Thus, to what extent the formation and presence of the poly(dA:rU) hybrid affects Pol III transcription termination cannot be directly answered with our cryo-EM analysis, as it would require us to capture Pol III being bound to poly(dT) and a poly(dA:rU) hybrid. Capturing this state will likely prove challenging because Pol III may terminate before or during cryo-EM sample preparation. Nevertheless, such analysis will be an important next step to understand the Pol III transcription termination mechanism in full detail.

STAR★METHODS

Detailed methods are provided in the online version of this paper and include the following:

- KEY RESOURCES TABLE
- RESOURCE AVAILABILITY

SUPPLEMENTAL INFORMATION

Supplemental information can be found online at https://doi.org/10.1016/j.celrep.2022.111316.

ACKNOWLEDGMENTS

We thank F. Weis and W.J.H. Hagen (EMBL Cryo-Electron Microscopy Service Platform) for EM support; T. Hoffmann and J. Pecar and EMBL IT Support for computational and data storage support, and T. Hoffmann and J. Pecar in particular for setting up and maintaining the high-performance computing environment; R.J. Maraia for sharing the yeast Pol III Δ expression strain; S.C. Vonesch for advice on CRISPR-Cas9-mediated genome engineering of yeast cells; F. Baudin for RNA labeling and advice on biochemical experiments; M.K. Vorländer for providing purified TFIIIB components and advice on cryo-EM data collection and processing; N.A. Hoffman for initial project discussions; and current members of the Müller lab for discussions. M.G., H.G., and C.W.M acknowledge support from EMBL. M.G. was supported by a Boehringer Ingelheim Fonds PhD fellowship. D.L. and O.P. were supported by the Agence National pour la Recherche (ANR-16-CE12-0001-01 to O.P. and ANR-16-CE12-0022-01 to D.L) and the Fondation pour la Recherche Medical (F.R.M., program Equipes 2019). J.X. was supported by the China Scholarship Council, the F.R.M. PhD fellowship (FDT202012010433), and LabEx "Who Am I?" (ANR-11-LABX-0071 and Université de Paris IdEx ANR-18-IDEX-0001) funded by the French government through its "Investments for the Future."

AUTHOR CONTRIBUTIONS

C.W.M. initiated and supervised the project. M.G. carried out protein purifications, biochemical experiments, cryo-EM grid preparation and data collections, and model building and interpreted the structures. H.G. performed genome engineering of yeast cells via CRISPR-Cas9, handled yeast cultures, and did yeast spotting assays. J.X. performed CRAC experiments. J.X., D.L., and O.P. analyzed and interpreted the CRAC results. M.G. wrote the manuscript with input from the other authors.

DECLARATION OF INTERESTS

The authors declare no competing interests.

Received: March 10, 2022
Revised: July 1, 2022
Accepted: August 15, 2022
Published: September 6, 2022

REFERENCES

Abascal-Palacios, G., Ramsay, E.P., Beuron, F., Morris, E., and Vannini, A. (2018). Structural basis of RNA polymerase III transcription initiation. Nature *553*, 301–306.

Alic, N., Ayoub, N., Landrieux, E., Favry, E., Baudouin-Cornu, P., Riva, M., and Carles, C. (2007). Selectivity and proofreading both contribute significantly to the fidelity of RNA polymerase III transcription. Proc. Natl. Acad. Sci. USA *104*, 10400–10405.

Allison, D.S., and Hall, B.D. (1985). Effects of alterations in the 3' flanking sequence on in vivo and in vitro expression of the yeast SUP4-o tRNATyr gene. EMBO J. *4*, 2657–2664.

Arimbasseri, A.G., and Maraia, R.J. (2013). Distinguishing core and holoenzyme mechanisms of transcription termination by RNA polymerase III. Mol. Cell Biol. *33*, 1571–1581.

Arimbasseri, A.G., and Maraia, R.J. (2015). Mechanism of transcription termination by RNA polymerase III utilizes a non-template strand sequence-specific signal element. Mol. Cell *58*, 1124–1132.

Barnes, C.O., Cohen, A.E., Brown, I.S., Zhang, Q., Graham, B.W., Spahr, H., Lin, G., Barnes, C.O., Calero, M., Malik, I., Pullara, F., et al. (2015). Crystal structure of a transcribing RNA polymerase II complex reveals a complete transcription bubble. Mol. Cell *59*, 258–269.

Beitz, E. (2000). TeXshade: shading and labeling of multiple sequence alignments using LaTeX2e. Bioinformatics *16*, 135–139.

Bogenhagen, D.F., and Brown, D.D. (1981). Nucleotide sequences in Xenopus 5S DNA required for transcription termination. Cell *24*, 261–270.

Bolger, A.M., Lohse, M., and Usadel, B. (2014). Trimmomatic: a flexible trimmer for Illumina sequence data. Bioinformatics *30*, 2114–2120.

Braglia, P., Percudani, R., and Dieci, G. (2005). Sequence context effects on oligo(dT) termination signal recognition by Saccharomyces cerevisiae RNA polymerase III. J. Biol. Chem. *280*, 19551–19562.

Brun, I., Sentenac, A., and Werner, M. (1997). Dual role of the C34 subunit of RNA polymerase III in transcription initiation. EMBO J. *16*, 5730–5741.

Candelli, T., Challal, D., Briand, J.B., Boulay, J., Porrua, O., Colin, J., and Libri, D. (2018). High-resolution transcription maps reveal the widespread impact of roadblock termination in yeast. EMBO J. *37*, e97490.

Casañal, A., Lohkamp, B., and Emsley, P. (2020). Current developments in Coot for macromolecular model building of electron cryo-microscopy and crystallographic data. Protein Sci. *29*, 1055–1064.

Challal, D., Barucco, M., Kubik, S., Feuerbach, F., Candelli, T., Geoffroy, H., Benaksas, C., Shore, D., and Libri, D. (2018). General regulatory factors control the fidelity of transcription by restricting non-coding and ectopic initiation. Mol. Cell *72*, 955–969.e7.

Chédin, S., Riva, M., Schultz, P., Sentenac, A., and Carles, C. (1998). The RNA cleavage activity of RNA polymerase III is mediated by an essential TFIIS-like subunit and is important for transcription termination. Genes Dev. *12*, 3857–3871.

Cheung, A.C.M., and Cramer, P. (2011). Structural basis of RNA polymerase II backtracking, arrest and reactivation. Nature *471*, 249–253.

Cozzarelli, N.R., Gerrard, S.P., Schlissel, M., Brown, D.D., and Bogenhagen, D.F. (1983). Purified RNA polymerase III accurately and efficiently terminates transcription of 5S RNA genes. Cell *34*, 829–835.

Croll, T.I. (2018). Isolde : a physically realistic environment for model building into low-resolution electron-density maps. Acta Crystallogr. D Struct. Biol. *74*, 519–530.

de la Rosa-Trevín, J.M., Quintana, A., del Cano, L., Zaldívar, A., Foche, I., Gutiérrez, J., Gómez-Blanco, J., Burguet-Castell, J., Cuenca-Alba, J., Abrishami,

V., et al. (2016). Scipion: a software framework toward integration, reproducibility and validation in 3D electron microscopy. J. Struct. Biol. *195*, 93–99.

Dieci, G., and Sentenac, A. (1996). Facilitated recycling pathway for RNA polymerase III. Cell *84*, 245–252.

Emsley, P., Lohkamp, B., Scott, W.G., and Cowtan, K. (2010). Features and development of Coot. Acta Crystallogr. D Biol. Crystallogr. *66*, 486–501.

Girbig, M., Misiaszek, A.D., Vorländer, M.K., Lafita, A., Grötsch, H., Baudin, F., Bateman, A., and Müller, C.W. (2021). Cryo-EM structures of human RNA polymerase III in its unbound and transcribing states. Nat. Struct. Mol. Biol. *28*, 210–219.

Goddard, T.D., Huang, C.C., and Ferrin, T.E. (2007). Visualizing density maps with UCSF Chimera. J. Struct. Biol. *157*, 281–287.

Goddard, T.D., Huang, C.C., Meng, E.C., Pettersen, E.F., Couch, G.S., Morris, J.H., and Ferrin, T.E. (2018). UCSF ChimeraX: meeting modern challenges in visualization and analysis. Protein Sci. *27*, 14–25.

Granneman, S., Kudla, G., Petfalski, E., and Tollervey, D. (2009). Identification of protein binding sites on U3 snoRNA and pre-rRNA by UV cross-linking and high-throughput analysis of cDNAs. Proc. Natl. Acad. Sci. USA *106*, 9613–9618.

Han, Y., Yan, C., Fishbain, S., Ivanov, I., and He, Y. (2018). Structural visualization of RNA polymerase III transcription machineries. Cell Discov. *4*, 40.

Hoffmann, N.A., Jakobi, A.J., Moreno-Morcillo, M., Glatt, S., Kosinski, J., Hagen, W.J.H., Sachse, C., and Müller, C.W. (2015). Molecular structures of unbound and transcribing RNA polymerase III. Nature *528*, 231–236.

Hou, H., Li, Y., Wang, M., Liu, A., Yu, Z., Chen, K., Zhao, D., and Xu, Y. (2021). Structural insights into RNA polymerase III-mediated transcription termination through trapping poly-deoxythymidine. Nat. Commun. *12*, 6135.

Iben, J.R., Mazeika, J.K., Hasson, S., Rijal, K., Arimbasseri, A.G., Russo, A.N., and Maraia, R.J. (2011). Point mutations in the Rpb9-homologous domain of Rpc11 that impair transcription termination by RNA polymerase III. Nucleic Acids Res. *39*, 6100–6113.

Jakobi, A.J., Wilmanns, M., and Sachse, C. (2017). Model-based local density sharpening of cryo-EM maps. Elife *6*, e27131.

James, P., and Hall, B.D. (1990). ret1-1, a yeast mutant affecting transcription termination by RNA polymerase III. Genetics *125*, 293–303.

Kassavetis, G.A., Prakash, P., and Shim, E. (2010). The C53/C37 subcomplex of RNA polymerase III lies near the active site and participates in promoter opening. J. Biol. Chem. *285*, 2695–2706.

Keeling, P.J., and Burki, F. (2019). Progress towards the tree of eukaryotes. Curr. Biol. *29*, R808–R817.

Kidmose, R.T., Juhl, J., Nissen, P., Boesen, T., Karlsen, J.L., and Pedersen, B.P. (2019). Namdinator – automatic molecular dynamics flexible fitting of structural models into cryo-EM and crystallography experimental maps. IUCrJ *6*, 526–531.

Landrieux, E., Alic, N., Ducrot, C., Acker, J., Riva, M., and Carles, C. (2006). A subcomplex of RNA polymerase III subunits involved in transcription termination and reinitiation. EMBO J. *25*, 118–128.

Langmead, B., and Salzberg, S.L. (2012). Fast gapped-read alignment with Bowtie 2. Nat. Methods *9*, 357–359.

Lefèvre, S., Dumay-Odelot, H., El-Ayoubi, L., Budd, A., Legrand, P., Pinaud, N., Teichmann, M., and Fribourg, S. (2011). Structure-function analysis of hRPC62 provides insights into RNA polymerase III transcription initiation. Nat. Struct. Mol. Biol. *18*, 352–358.

Li, L., Yu, Z., Zhao, D., Ren, Y., Hou, H., and Xu, Y. (2021). Structure of human RNA polymerase III elongation complex. Cell Res. *31*, 791–800.

Liebschner, D., Afonine, P.V., Baker, M.L., Bunkóczi, G., Chen, V.B., Croll, T.I., Hintze, B., Hung, L.-W., Jain, S., McCoy, A.J., et al. (2019). Macromolecular structure determination using X-rays, neutrons and electrons: recent developments in Phenix. Acta Crystallogr. D Struct. Biol. *75*, 861–877.

Martin, F.H., and Tinoco, I. (1980). DNA-RNA hybrid duplexes containing oligo(dA:rU) sequences are exceptionally unstable and may facilitate termination of transcription. Nucleic Acids Res. *8*, 2295–2299.

Mastronarde, D.N. (2005). Automated electron microscope tomography using robust prediction of specimen movements. J. Struct. Biol. *152*, 36–51.

Mishra, S., and Maraia, R.J. (2019). RNA polymerase III subunits C37/53 modulate rU:dA hybrid 3′ end dynamics during transcription termination. Nucleic Acids Res. *47*, 310–327.

Mishra, S., Hasan, S.H., Sakhawala, R.M., Chaudhry, S., and Maraia, R.J. (2021). Mechanism of RNA polymerase III termination-associated reinitiation-recycling conferred by the essential function of the N terminal-and-linker domain of the C11 subunit. Nat. Commun. *12*, 5900.

Morin, A., Eisenbraun, B., Key, J., Sanschagrin, P.C., Timony, M.A., Ottaviano, M., and Sliz, P. (2013). Collaboration gets the most out of software. Elife *2*, e01456.

Nicholls, R.A., Long, F., and Murshudov, G.N. (2012). Low-resolution refinement tools in REFMAC 5. Acta Crystallogr. D Biol. Crystallogr. *68*, 404–417.

Notredame, C., Higgins, D.G., and Heringa, J. (2000). T-coffee: a novel method for fast and accurate multiple sequence alignment 1 1Edited by. J. Mol. Biol. *302*, 205–217.

Porrua, O., and Libri, D. (2015). Transcription termination and the control of the transcriptome: why, where and how to stop. Nat. Rev. Mol. Cell Biol. *16*, 190–202.

Punjani, A., Rubinstein, J.L., Fleet, D.J., and Brubaker, M.A. (2017). cryoSPARC: algorithms for rapid unsupervised cryo-EM structure determination. Nat. Methods *14*, 290–296.

Quinlan, A.R., and Hall, I.M. (2010). BEDTools: a flexible suite of utilities for comparing genomic features. Bioinformatics *26*, 841–842.

Ramírez, F., Ryan, D.P., Grüning, B., Bhardwaj, V., Kilpert, F., Richter, A.S., Heyne, S., Dündar, F., and Manke, T. (2016). deepTools2: a next generation web server for deep-sequencing data analysis. Nucleic Acids Res. *44*, W160–W165.

Ramírez-Aportela, E., Vilas, J.L., Glukhova, A., Melero, R., Conesa, P., Martínez, M., Maluenda, D., Mota, J., Jiménez, A., Vargas, J., et al. (2019). Automatic local resolution-based sharpening of cryo-EM maps. Bioinformatics *36*, 765–772.

Ramsay, E.P., Abascal-Palacios, G., Daiß, J.L., King, H., Gouge, J., Pilsl, M., Beuron, F., Morris, E., Gunkel, P., Engel, C., and Vannini, A. (2020). Structure of human RNA polymerase III. Nat. Commun. *11*, 6409.

Richard, P., and Manley, J.L. (2009). Transcription termination by nuclear RNA polymerases. Genes Dev. *23*, 1247–1269.

Rijal, K., and Maraia, R.J. (2013). RNA polymerase III mutants in TFIIFα-like C37 that cause terminator readthrough with no decrease in transcription output. Nucleic Acids Res. *41*, 139–155.

Rijal, K., and Maraia, R.J. (2016). Active center control of termination by RNA polymerase III and tRNA gene transcription levels in vivo. PLoS Genet. *12*, e1006253.

Rivosecchi, J., Larochelle, M., Teste, C., Grenier, F., Malapert, A., Ricci, E.P., Bernard, P., Bachand, F., and Vanoosthuyse, V. (2019). Senataxin homologue Sen1 is required for efficient termination of RNA polymerase III transcription. EMBO J. *38*, e101955.

Rosenthal, P.B., and Henderson, R. (2003). Optimal determination of particle orientation, absolute hand, and contrast loss in single-particle electron cryomicroscopy. J. Mol. Biol. *333*, 721–745.

Shaaban, S.A., Bobkova, E.V., Chudzik, D.M., and Hall, B.D. (1996). In vitro analysis of elongation and termination by mutant RNA polymerases with altered termination behavior. Mol. Cell Biol. *16*, 6468–6476.

Shaaban, S.A., Krupp, B.M., and Hall, B.D. (1995). Termination-altering mutations in the second-largest subunit of yeast RNA polymerase III. Mol. Cell Biol. *15*, 1467–1478.

Tafur, L., Sadian, Y., Hoffmann, N.A., Jakobi, A.J., Wetzel, R., Hagen, W.J.H., Sachse, C., and Müller, C.W. (2016). Molecular structures of transcribing RNA polymerase I. Mol. Cell *64*, 1135–1143.

Tegunov, D., and Cramer, P. (2019). Real-time cryo-electron microscopy data preprocessing with Warp. Nat. Methods *16*, 1146–1152.

Thomas, M.J., Platas, A.A., and Hawley, D.K. (1998). Transcriptional fidelity and proofreading by RNA polymerase II. Cell *93*, 627–637.

Thuillier, V., Stettler, S., Sentenac, A., Thuriaux, P., and Werner, M. (1995). A mutation in the C31 subunit of Saccharomyces cerevisiae RNA polymerase III affects transcription initiation. EMBO J. *14*, 351–359.

Turowski, T.W., Leśniewska, E., Delan-Forino, C., Sayou, C., Boguta, M., and Tollervey, D. (2016). Global analysis of transcriptionally engaged yeast RNA polymerase III reveals extended tRNA transcripts. Genome Res. *26*, 933–944.

Valdar, W.S. (2002). Scoring residue conservation. Proteins *48*, 227–241.

Vilas, J.L., Gómez-Blanco, J., Conesa, P., Melero, R., Miguel de la Rosa-Trevín, J., Otón, J., Cuenca, J., Marabini, R., Carazo, J.M., Vargas, J., and Sorzano, C.O.S. (2018). MonoRes: automatic and accurate estimation of local resolution for electron microscopy maps. Structure *26*, 337–344.e4.

Vorländer, M.K., Baudin, F., Moir, R.D., Wetzel, R., Hagen, W.J.H., Willis, I.M., and Müller, C.W. (2020). Structural basis for RNA polymerase III transcription repression by Maf1. Nat. Struct. Mol. Biol. *27*, 229–232.

Vorländer, M.K., Khatter, H., Wetzel, R., Hagen, W.J.H., and Müller, C.W. (2018). Molecular mechanism of promoter opening by RNA polymerase III. Nature *553*, 295–300.

Wang, Q., Li, S., Wan, F., Xu, Y., Wu, Z., Cao, M., Lan, P., Lei, M., and Wu, J. (2021). Structural insights into transcriptional regulation of human RNA polymerase III. Nat. Struct. Mol. Biol. *28*, 220–227.

Wang, Z., and Roeder, R.G. (1997). Three human RNA polymerase III-specific subunits form a subcomplex with a selective function in specific transcription initiation. Genes Dev. *11*, 1315–1326.

Waterhouse, A.M., Procter, J.B., Martin, D.M.A., Clamp, M., and Barton, G.J. (2009). Jalview Version 2--a multiple sequence alignment editor and analysis workbench. Bioinformatics *25*, 1189–1191.

Watson, J.B., Chandler, D.W., and Gralla, J.D. (1984). Specific termination of in vitro transcription by calf thymus RNA polymerase III. Nucleic Acids Res. *12*, 5369–5384.

Webb, S., Hector, R.D., Kudla, G., and Granneman, S. (2014). PAR-CLIP data indicate that Nrd1-Nab3-dependent transcription termination regulates expression of hundreds of protein coding genes in yeast. Genome Biol. *15*, R8.

Xie, J., Aiello, U., Clement, Y., Haidara, N., Girbig, M., Schmitzova, J., Pena, V., Müller, C.W., Libri, D., and Porrua, O. (2022). An integrated model for termination of RNA polymerase III transcription. Sci. Adv. *8*, eabm9875.

Zhang, K. (2016). Gctf: real-time CTF determination and correction. J. Struct. Biol. *193*, 1–12.

Zheng, S.Q., Palovcak, E., Armache, J.-P., Verba, K.A., Cheng, Y., and Agard, D.A. (2017). MotionCor2: anisotropic correction of beam-induced motion for improved cryo-electron microscopy. Nat. Methods *14*, 331–332.

Zivanov, J., Nakane, T., Forsberg, B.O., Kimanius, D., Hagen, W.J., Lindahl, E., and Scheres, S.H. (2018). New tools for automated high-resolution cryo-EM structure determination in RELION-3. Elife *7*, e42166.

STAR★METHODS

KEY RESOURCES TABLE

REAGENT or RESOURCE	SOURCE	IDENTIFIER
Antibodies		
IgG from rabbit serum	Sigma-Aldrich	Cat# I5006; RRID: AB_1163659
Bacterial and virus strains		
Escherichia coli XL1-Blue chemically competent cells	Agilent	200249
Chemicals, peptides, and recombinant proteins		
Tris	Sigma	T1503
HCl	Merck	1.00319
Ammonium sulfate	Applichem	A1032
Glycerol	Merck	1.04057
Lithium acetate (CH_3COOLi)	Sigma	62393
EDTA	Merck	E5134
$MgCl_2$	Sigma	M9272
$ZnCl_2$	Sigma	39059
ß-mercaptoethanol	Aldrich	M6250
DTT	Biomol	04010
Leupeptin	Sigma	11017128001
Pepstatin A	Applichem	A2205
PMSF	Sigma	P7626
Benzamidin	Merck	12072
Hepes	Merck	H23830
Imidazole	Sigma	56750
$MgSO_4$	Merck	S0505
Sodium acetate (CH_3COONa)	Merck	236500
Urea	Merck	1.08487
Ethanol	Merck	1.00983
Nourseothricin (clonNAT)	Jena Bioscience	AB-102L
Ampicillin	Applichem	A0839
DMSO	Sigma	D2438
Betaine	Sigma	B0300
PEG 4000	Merck	95904
Boric acid	Merck	B6768
Salmon sperm DNA	Thermofisher	15632011
NTP (ATP, CTP, GTP, UTP)	Thermofisher	R0481
[α-P32]UTP (10 mCi/ml)	Hartmann Analytic	FP-110
[γ-P32]ATP (10 mCi/mL)	Hartmann Analytic	FP-201
Formamide	Merck	F9037
Glycogen	ThermoFisher Scientific	10814010
Phenol–chloroform	Applichem	A0889
T4 PNK	Biolabs	M0201L
T7 ligase	Biolabs	M0318S
BsmBI	Thermofisher	ER0451
Phusion DNA Polymerase	Thermofisher	F530L
DpnI	ThermoScientific	FD1704

(*Continued on next page*)

Continued

REAGENT or RESOURCE	SOURCE	IDENTIFIER
Bradford reagent	ThermoScientific	23200
cOmplete EDTA-free protease inhibitor cocktail tablets	Sigma-Aldrich (Roche)	Cat# 11873580001
Dnase I recombinant, Rnase-free	Sigma-Aldrich (Roche)	Cat# 04716728001
Dynabeads M-280 Tosylactivated	Thermo Fisher Scientific	Cat# 14204
Recombinant GST-TEV protease	(Challal et al., 2018)	N/A
Rnace-It Ribonuclease Cocktail	Agilent	Cat# 400720
Guanidine hydrochloride	Sigma-Aldrich	Cat# G4505
Ni-NTA Agarose	QIAGEN	Cat# 30230
RNaseOUT Recombinant Ribonuclease Inhibitor	Thermo Fisher Scientific	Cat# 10777019
T4 RNA Ligase 2, truncated KQ	NEB	Cat# M0373L
T4 RNA Ligase 1 (ssRNA Ligase)	NEB	Cat# M0204L
Proteinase K, recombinant, PCR grade	Sigma-Aldrich (Roche)	Cat# 03115887001
SuperScript IV Reverse Transcriptase	Thermo Fisher Scientific	Cat# 18090050
Rnase H	NEB	Cat# M0297S
Exonuclease I	NEB	Cat# M0293S
LA Taq	Takara	Cat# RR002M
Critical commercial assays		
LightCycler 480 SYBR Green I Master	Roche	Cat# 04887352001
NucleoSpin Gel and PCR Clean-up	Macherey-Nagel	Cat# 740609
Pierce Spin Columns - Snap Cap	Thermo Fisher Scientific	Cat# 69725
Vivacon 500	Sartorius	Cat# VN01H22
Qubit dsDNA HS Assay Kit	Thermo Fisher Scientific (Invitrogen)	Cat# Q32851
SuperSignal West Pico Chemiluminescent Substrate	Thermo Fisher Scientific	Cat# 34080
Deposited data		
Atomic coordinates of yeast Pol III PTC	This paper	PDB: 7Z1L
Cryo-EM map of yeast Pol III PTC (Map A)	This paper	EMDB: EMD-14447
Atomic coordinates of yeast Pol III EC	This paper	PDB: 7Z1M
Cryo-EM map of yeast Pol III EC (Map B)	This paper	EMDB: EMD-14448
Atomic coordinates of yeast Pol III Δ	This paper	PDB: 7Z1N
Cryo-EM map of yeast Pol III Δ (Map C)	This paper	EMDB: EMD-14449
Atomic coordinates of yeast Pol III PTC + NTPs	This paper	PDB: 7Z1O
Cryo-EM map of yeast Pol III PTC + NTPs (Map D)	This paper	EMDB: EMD-14451
Cryo-EM map of yeast Pol III PTC + NTPs 2 (Map E)	This paper	EMDB: EMD-14450
Genome-wide data	This paper	GEO: GSE196398
Experimental models: Organisms/strains		
AC40-TAP-tagged *S. cerevisiae* strain to purify Pol III WT (large scale); genotype: SC0000; MATa; ade2; arg4; leu2-3,112; trp1-289; ura3-52; YPR110c::TAP-KlURA3	Cellzome GmbH	Euroscarf #SC1613
C128-TAP-tagged *S. cerevisiae* strain to purify Pol III WT (small scale); genotype: MATa; ade2; arg4; leu2-3,112 trp1-289; ura3-52; YOR207c::TAP-KlURA3	Cellzome GmbH	Euroscarf #SC2330

(*Continued on next page*)

Continued

REAGENT or RESOURCE	SOURCE	IDENTIFIER
His_6-$FLAG_3$-C128-tagged *S. cerevisiae* strain to purify Pol III Δ; genotype: ret1::URA3MX, pRS313:N-His-FLAG-C128; rpo31D::KanMX, pRS313gu-nHA-C160, rpc11D::NatMX, ppRS316gu-spC11mvq	Maraia lab (NIH/NICHD, Bethesda), original citation: Kassavetis et al., 2010 (https://doi.org/10.1074/jbc.M109.074013)	N/A
C128-TAP-tagged *S. cerevisiae* strain to purify Pol III C128 triple mutant; genotype: MATa; ade2; arg4; leu2-3,112 trp1-289; ura3-52; YOR207c_Q476A, K479A, R481G::TAP-KlURA3	This paper	N/A
C128-TAP-tagged *S. cerevisiae* strain to purify Pol III C128 Q199R mutant; genotype: MATa; ade2; arg4; leu2-3,112 trp1-289; ura3-52; YOR207c_Q199R::TAP-KlURA3	This paper	N/A
C128-TAP-tagged *S. cerevisiae* strain to purify Pol III C128 R451V mutant; genotype: MATa; ade2; arg4; leu2-3,112 trp1-289; ura3-52; YOR207c_ R451V::TAP-KlURA3	This paper	N/A
C128-TAP-tagged *S. cerevisiae* strain to purify Pol III C128 K448A mutant; genotype: MATa; ade2; arg4; leu2-3,112 trp1-289; ura3-52; YOR207c_ K448A::TAP-KlURA3	This paper	N/A
C128-TAP-tagged *S. cerevisiae* strain to purify Pol III C128 R481G mutant; genotype: MATa; ade2; arg4; leu2-3,112 trp1-289; ura3-52; YOR207c_ R481G::TAP-KlURA3	This paper	N/A
C128-TAP-tagged *S. cerevisiae* strain to purify Pol III C128 H225L mutant; genotype: MATa; ade2; arg4; leu2-3,112 trp1-289; ura3-52; YOR207c_ H225L::TAP-KlURA3	This paper	N/A
His_6TAP-TRP1-tagged *S. cerevisiae* strain for CRAC, C128 WT; genotype: MATa, ade2, arg4, leu2-3, 112, trp1-289, ura3-52, YOR207c_WT, YOR116c::His_6TAP-TRP1	This paper	N/A
His_6TAP-TRP1-tagged *S. cerevisiae* strain for CRAC, C128 triple mutant; genotype: MATa, ade2, arg4, leu2-3, 112, trp1-289, ura3-52, YOR207c_Q476A, K479A, R481G::TAP-KlURA3	This paper	N/A
His_6TAP-TRP1-tagged *S. cerevisiae* strain for CRAC, C128 Q199R mutant; genotype: MATa, ade2, arg4, leu2-3, 112, trp1-289, ura3-52, YOR207c_Q199R, YOR116c::His_6TAP-TRP1	This paper	N/A
His_6TAP-TRP1-tagged *S. cerevisiae* strain for CRAC, C128 R451V mutant; genotype: MATa, ade2, arg4, leu2-3, 112, trp1-289, ura3-52, YOR207c_R451V, YOR116c::His_6TAP-TRP1	This paper	N/A
Oligonucleotides		
Oligonucleotides are listed in Table S2.		N/A
Recombinant DNA		
Plasmid: pWS082	Addgene	90516
Plasmid: pWS174	Addgene	90961

(*Continued on next page*)

Continued

REAGENT or RESOURCE	SOURCE	IDENTIFIER
Software and algorithms		
BEDTools	Quinlan and Hall, 2010	https://bedtools.readthedocs.io/en/latest/
Bowtie 2	Langmead and Salzberg, 2012	https://sourceforge.net/projects/bowtie-bio/files/bowtie2/
Coot 0.8.9.1	Emsley et al., 2010	https://www2.mrc-lmb.cam.ac.uk/personal/pemsley/coot/
cryoSPARC 2.15.0	Punjani et al., 2017	https://cryosparc.com/
deepTools	Ramírez et al., 2016	https://deeptools.readthedocs.io/en/develop/
FASTX-Toolkit	Hannon lab CSHL	http://hannonlab.cshl.edu/fastx_toolkit/
Image Lab	Bio-Rad	https://www.bio-rad.com/de-de/product/image-lab-software?ID=KRE6P5E8Z
ISOLDE 1.0	Croll, 2018	https://isolde.cimr.cam.ac.uk/
Jalview 2.11.0	Waterhouse et al., 2009	http://www.jalview.org/getdown/release/
LocalDeblur	Ramírez-Aportela et al., 2019	https://github.com/I2PC/xmipp
MonoRes	Vilas et al., 2018	https://github.com/I2PC/xmipp
pyCRAC	Webb et al., 2014	https://git.ecdf.ed.ac.uk/sgrannem/pycrac
PHENIX 1.19	Liebschner et al., 2019	https://phenix-online.org/
RELION 3.1	Zivanov et al., 2018	https://relion.readthedocs.io/en/release-3.1/
R 3.5.3	R Core Team	https://www.R-project.org
RStudio 1.1.456	RStudio Team	https://www.rstudio.com/
Scipion 2.0	de la Rosa-Trevín et al., 2016	http://scipion.cnb.csic.es/
SerialEM 3.8.0 beta	Mastronarde, 2005	https://bio3d.colorado.edu/SerialEM/
TeXshade 1.25	Beitz, 2000	https://ctan.net/macros/latex/contrib/texshade/
T-Coffee	Notredame et al., 2000	https://www.ebi.ac.uk/Tools/msa/tcoffee/
Trimmomatic	Bolger et al., 2014	http://www.usadellab.org/cms/index.php?page=trimmomatic
UCSF Chimera	Goddard et al., 2007	https://www.cgl.ucsf.edu/chimera/
UCSF ChimeraX	Goddard et al., 2018	https://www.cgl.ucsf.edu/chimerax/
Warp 1.0.6	Tegunov and Cramer, 2019	https://isolde.cimr.cam.ac.uk/

RESOURCE AVAILABILITY

Lead contact

Further information and requests for resources and reagents should be directed to and will be fulfilled by the lead contact, Christoph W. Müller (christoph.mueller@embl.de).

Materials availability

Plasmids and yeast strains are available upon request and will be available without restrictions.

Data and code availability

- Atomic coordinates and cryo-EM maps of the Pol III PTC, Pol III EC, Pol III Δ and Pol III PTC + NTPs have been deposited to the Protein Data Bank (PDB) and to the Electron Microscopy Data Base (EMDB) under the following accession codes: yeast Pol III PTC: PDB: 7Z1L, EMDB: EMD-14447; yeast Pol III EC: PDB: 7Z1M, EMDB: EMD-14448; yeast Pol III Δ: PDB: 7Z1N, EMDB: EMD-14449; yeast Pol III PTC + NTPs: PDB: 7Z1O, EMDB: EMD-14451; Pol III PTC + NTPs 2 (classified on nucleic acids): EMDB: EMD-14450. CRAC data has been deposited to the NCBI's Gene Expression Omnibus (GEO) under accession code GEO: GSE196398.
- This paper does not report original code.
- Any additional information required to reanalyze the data reported in this paper is available from the lead contact upon request

EXPERIMENTAL MODEL AND SUBJECT DETAILS

Yeast strains

Yeast cells were grown in YPAD, YPD, YPGAL or CSM-TRP medium and, if not otherwise stated, grown at a temperature of 30°C. Growth conditions for yeast cells strains varied between experiments and are, therefore, further specified in the Method details section. The genotypes for the used yeast strains can be found in the Key resources table.

METHOD DETAILS

Large scale purification of endogenous Pol III

Yeast Pol III was purified in large scale from a *S. cerevisiae* strain (Euroscarf ID #SC1613) carrying a C-terminal TAP-tag on subunit AC40. Large-scale purified Pol III was used for structural analysis and biochemical experiments. Yeast cells were grown in a 100 L fermenter (BIOSTAT® D-DCU, Sartorius) in YPAD medium for 17 h at 30°C. Cells were harvested in log phase ($OD_{600\ nm}$ > 6.5) with a flow-through centrifuge, which typically yielded a ca. 1.5 kg cell pellet that was kept at −80°C until usage. For purification, the yeast cell pellet was thawed over night at 4°C and, the next day, washed with cell wash buffer (50 mM Tris-HCl pH 8 (RT), 250 mM $(NH_4)_2SO_4$, 12 mM β-mercaptoethanol) by dissolving the yeast pellet in 100 mL wash buffer per 100 g cell pellet and centrifugation (JLA 8.1000 rotor, Beckman) at 5,000 rpm, 4°C for 10 min. The supernatant was removed and the cell pellet was resuspended in lysis buffer (250 mM Tris-HCl pH 8 (RT), 20% glycerol, 250 mM $(NH_4)_2SO_4$, 1 mM EDTA, 10 mM $MgCl_2$, 10 μM $ZnCl_2$, 12 mM mercaptoethanol), supplemented with protease inhibitor (PI) cocktail mix (0.3 μg/mL Leupeptin, 1.4 μg/mL Pepstatin, 170 μg/mL PMSF, 330 μg/mL benzamidin, in EtOH). For cell lysis, all material and equipment was pre-cooled at 4°C and lysis steps were performed at 4°C. Cells were lysed with glass beads in a bead beater (BioSpec) using ca. 230 mL cell suspension per beaker (ca. 6 beakers in total) and 170 mL glass beads per beaker, supplemented with a spatula tip of Pefabloc. Beakers were cooled using an ice-salty water (5 M NaCl) bath. Cells were lysed by beating 8 times for 45 s and waiting for 90 s. The lysate was filtered through a metal mesh and centrifuged (JA-14 rotor, Beckman) at 14,000 rpm, 4°C for 1 h. The supernatant was recovered, filtered again through a metal mesh and applied to a 350 mL heparin sepharose (GE Healthcare) column equilibrated in HEP bind buffer (50 mM Tris-HCl pH 8 (RT), 20% glycerol, 250 mM $(NH_4)_2SO_4$, 0.5 mM EDTA, 1 mM $MgCl_2$, 10 μM $ZnCl_2$, 1 mM β-mercaptoethanol), supplemented with PI mix (see above). The remaining cell pellet (containing unlysed yeast cells) was resuspended in lysis buffer, lysed again using the procedure described above, and also applied to the heparin column. Bound proteins were eluted using a 400 mL linear gradient (0–100%) from buffer HEP A (50 mM Tris-HCl pH 8 (RT), 250 mM $(NH_4)_2SO_4$, 0.5 mM EDTA, 1 mM $MgCl_2$, 10 μM $ZnCl_2$, 1 mM β-mercaptoethanol, PI mix) into HEP B (50 mM Tris-HCl pH 8 (RT), 1 M $(NH_4)_2SO_4$, 0.5 mM EDTA, 1 mM $MgCl_2$, 10 μM $ZnCl_2$, 1 mM β-mercaptoethanol, 0.5 mM PMSF). The eluate was diluted with HEP A buffer to 500 mM $(NH_4)_2SO_4$ and incubated with 20 mL IgG sepharose beads (GE Healthcare), equilibrated by washing with first 0.5 M AcOH pH 3.4 and second 1M Tris-HCl pH 7.5 (RT) (repeated twice) 4°C, rolling over night. The next day, beads were washed with 200 mL IgG binding buffer (50 mM Tris–HCl pH 8, 10% glycerol, 225 mM $(NH_4)_2SO_4$, 0.5 mM EDTA, 1 mM $MgCl_2$, 10 μM $ZnCl_2$, 2 mM β-mercaptoethanol), and bound proteins were eluted via addition of Tobacco etch virus (TEV) protease, incubation for 6 h at 4°C, and recovery of the supernatant. 100 mL of IgG elution buffer (50 mM Tris–HCl pH 8, 60 mM $(NH_4)_2SO_4$, 0.5 mM EDTA, 1 mM $MgCl_2$, 10 μM $ZnCl_2$, 2 mM β-mercaptoethanol) were added to the IgG beads and the flow-through was recovered and pooled with the first eluate. The eluted protein solution was applied to a MonoQ 10/100 column (Sigma-Aldrich, Merck), equilibrated in MonoQ buffer A (40 mM Hepes, pH 7.5, 60 mM $(NH_4)_2SO_4$, 0.5 mM EDTA, 1 mM $MgCl_2$, 10 μM $ZnCl_2$, 10 mM DTT). Bound proteins were eluted via linear gradient from 60 to 1000 mM $(NH_4)_2SO_4$ in buffer and buffer exchanged into EM buffer (15 mM Hepes, pH 7.5, 150 mM $(NH_4)_2SO_4$, 10 mM DTT). The protein sample was concentrated to 7.5–14.9 mg/mL, snap-frozen in liquid nitrogen and stored at −80°C until usage.

Small scale purification of endogenous Pol III

Yeast Pol III was purified in small scale for structure-function studies from either a *S. cerevisiae* strain (Euroscarf ID #SC2330) carrying a C-terminal TAP-tag on subunit C128 (Pol III WT) or from *S. cerevisiae* mutant strains, genome-engineered via CRISPR-Cas9 (see below). Yeast cells were grown in 24 L cultures (in YPD medium) in conical flasks. To do so, 30 mL of yeast over-night cultures were prepared and diluted to 100 mL the next morning. In the evening, the cultures were diluted to 500 mL. The next day, the cultures were diluted to an $OD_{600\ nm}$ of 0.2, split amongst 16 × 1.5 L cultures and grown to an $OD_{600\ nm}$ of 1.5. The cultures were harvested by centrifugation (JLA 8.1000 rotor, Beckman, 3000 rpm, 10 min), washed once with PBS, and snap frozen in liquid nitrogen. Frozen cells (ca. 50 g per 24 L) were thawed over night at 4°C and resuspended in lysis buffer (see above), supplemented with PI mix (see above). The cells were lysed as described above. The lysate was cleared via centrifugation and loaded on two 5 mL HiTrap Heparin HP (Cytiva, Merck) columns (connected in series) that were equilibrated in lysis buffer. Proteins were eluted using a 100 mL linear gradient (0.25 to 1 M $(NH_4)_2SO_4$). Pol III was further purified as described above except that the MonoQ step was omitted. Buffer-exchanged proteins were concentrated up to 0.4 to 5.6 mg/mL, snap frozen, and stored at −80 °C.

Purification of yeast Pol III Δ

Pol III Δ (lacking C53/C37/C11) was purified for structural analysis from an *S. cerevisiae* strain harboring a His_6-tag on subunit C128. The strain was a gift from Richard Maraia (National Institutes of Health, Bethesda,MD, USA) and features a substitution of

endogenous *S. cerevisiae* C11 with *S. pombe* C11, which causes loss of the C53/C37 heterodimer upon protein purification (Kassavetis et al., 2010). Yeast cells were grown in a 100 L fermenter culture in YPGAL medium to an $OD_{600\ nm}$ of ca. 5.0–6.0. A 330 g pellet of frozen cells was thawed over night at 4°C and resuspended in lysis buffer (60 mM Hepes pH 7.5, 750 mM NaCl, 10.5 mM $MgCl_2$, 7.5% glycerol, 14.3 mM mercaptoethanol), supplemented with PI mix (see above). The cells were lysed as described above. The lysate was cleared via two centrifugation runs (1 h, 4°C, each): first run at 30,000 g; second run at 72,465 g. The lysate was loaded overnight onto a 5 mL HisTrap HP column (Cytiva, Merck) equilibrated in 20 mM Hepes pH 7.5, 500 mM NaCl, 7 mM $MgCl_2$, 10% glycerol, 10 mM mercaptoethanol, 10 mM imidazole). Bound proteins were eluted using a 100 mL linear gradient (10 to 300 mM imidazole), diluted with 120 mL of MonoQ buffer (40 mM Tris-HCl pH 8, 68 mM $(NH_4)_2SO_4$, 0.5 mM EDTA, 1 mM $MgCl_2$, 10 μM $ZnCl_2$, 10 mM DTT) and loaded onto a MonoQ 5/50 column (Sigma-Aldrich, Merck). Bound proteins were eluted using a 30 CV linear gradient (68 mM to 1 M $(NH_4)_2SO_4$), diluted with MonoQ A buffer, and applied a second time to the Mono Q 5/50 GL to increase purity. For the second elution step, a two-step linear gradient (first step: 68 mM to 250 mM $(NH_4)_2SO_4$; second step: 250 mM to 1 M $(NH_4)_2SO_4$) was used. Eluted proteins were buffer exchanged as described above, concentrated to 2.4 mg/mL, snap-frozen in liquid nitrogen and stored at −80°C until usage.

Preparation of transcription scaffolds

Transcription scaffolds were always prepared freshly before usage. Scaffolds used for cryo-EM sample preparation were annealed in a thermocycler (Bio-Rad) in the following way: oligonucleotides were dissolved in water. 1 μL of the template-strand and 1 μL of the non-template strand (100 μM each) were mixed and incubated at 95°C for 3 min. The temperature was incrementally reduced to 25°C at a rate of 1°C/min and 3 μL of 2× hybridization buffer (2xHB) (40 mM Hepes pH 7.5, 24 mM $MgCl_2$, 200 mM NaCl, 20 mM DTT) were added. 1 μL of the RNA strand (100 μM) were pre-heated at 45°C for 3 min and added to the mixture, which was incubated at 45°C for 3 min. The temperature was reduced to 20°C at a rate of 0.7°C/min, and the annealed scaffold was kept on ice.

Cryo-EM sample preparation

All samples were diluted to the working concentrations using EM buffer (15 mM Hepes, pH 7.5, 150 mM $(NH_4)_2SO_4$, 5 mM $MgCl_2$, 10 mM DTT), supplemented with 4 mM (final concentration) CHAPSO. For assembly of the nucleic-acid bound complexes, Pol III protein samples were incubated at 4°C for 60 min with 1.05× molar excess of pre-annealed transcription scaffolds (see above). The following final protein concentrations were used: 2.5 μM (Pol III PTC); 2.8 μM (Pol III EC); 3.4 μM (Pol III PTC + NTPs), 2.6 μM (Pol III Δ). For the Pol III PTC + NTPs sample, the EM buffer was further supplemented with CTP, ATP, and UTP (10 mM each) and the Pol III-nucleic acid complex was incubated for 90- instead of 60 min. After incubation with transcription scaffolds, 3 μL of sample was applied to 200-mesh copper R2/1 grids (Quantifoil), which were glow-discharged twice using a Pelco EasyGlow instrument. The cryo-EM grids were prepared at 100% humidity and 4°C using a Vitrobot Mark IV (Thermo Fisher Scientific) and the following blotting parameters: wait time 10 s, blot force 4, blot time 4 s. For cryo-EM sample preparation of Pol III Δ, a slightly different protocol was used: the DNA:RNA hybrid was first pre-annealed in a thermocycler by mixing 1 μL of T-DNA and 1 μL of RNA (100 μM each) using the same program as for the other annealing steps. After annealing, the DNA:RNA hybrid was diluted to a concentration of 12 μM in HB buffer (20 mM Hepes pH 7.5, 12 mM $MgCl_2$, 100 mM NaCl, 10 mM DTT). Next, 9 μL of Pol III Δ protein sample (c = 4 μM) were mixed with 3 μL DNA:RNA hybrid (c = 12 μM), and the mixture was incubated at 28 °C for 10 min. Afterwards, 1 μL of NT-DNA (c = 40 μM, diluted in HB buffer) strand was added, and the reaction was incubated for another 10 min at 28 °C before supplementing the mixture with 4 mM CHAPSO (final concentration) and plunge freezing as described above.

Cryo-EM data collection and processing

SerialEM (Mastronarde, 2005) was used for automated data collection. Cryo-EM data were collected on a Titan Krios transmission electron microscope (TEM) operated at 300 keV (Thermo Fisher Scientific), equipped with a Quantum energy filter (Gatan), and with a K2 (for Pol III PTC, EC and PTC + NTPs) or K3 (for Pol III Δ) direct detector (Gatan). Cryo-EM data collection parameters (magnification, pixel size, number of collected movies, movie frames, exposure time, dose, defocus range) for the four datasets are specified in Table S1. Warp (Tegunov and Cramer, 2019) was used for initial frame-alignment, dose-weighting, estimation of the contrast transfer function (CTF) and particle picking. The data was further processed in RELION 3.1 (Zivanov et al., 2018). For particle polishing, frame-alignment and dose-weighting was also done via RELION's own implementation of the MotionCor2-algorithm (Zheng et al., 2017) and CTF-correction was done with Gctf (Zhang, 2016). CryoSPARC (Punjani et al., 2017) was also used at earlier stages of image processing to assess data quality via 2D classification and generation of a 3D ab-initio reconstruction of the Pol III PTC, which was later used as a reference for 3D classification in RELION. Particle numbers and data processing steps are outlined in Figures S2, S3, S5, and S6. Following global 3D classification (4–6 classes, T value = 4), selected particles were subjected to 3D auto-refinement. Derived 3D maps were used to create global masks, covering the entire Pol III molecules, which were used for RELION post-processing and subsequent masked 3D classification. Masked 3D classification was performed without image alignment, with two classes, and a T value of 20. Masked 3D classification using a global mask enabled separation of Pol III molecules with and without the C53-C37 heterodimer and, typically, yielded slightly improved resolution values for the classes containing the complete Pol III molecule (with C53-C37). In the case of the Pol III PTC, masked 3D classification was repeated using a mask that covered only the C53-C37 heterodimer. Subsequently, particle images were CTF-refined and subjected to particle polishing in RELION. For particle polishing, selected particle images were first re-extracted from 3D movies, pre-processed in RELION (see above), and subjected to 3D auto-refinement. Next, we subjected the selected particle images

to iterative CTF refinement using: i) beam tilt estimation, trefoil estimation, 4th order aberrations estimation, ii) anisotropic magnification estimation; and iii) CTF parameter fitting using 'per particle' defocus fitting and 'per micrograph' astigmatism fitting. For particle polishing, optimal parameters were first trained using 5000 particles. Polished particles were again subjected to 3D auto-refinement, following iterative CTF refinement performed as described above and a final 3D auto-refinement run, which yielded the final 3D reconstructions used for map sharpening and atomic model building. In case of the Pol III PTC + NTPs dataset, the region corresponding to the upstream DNA was better resolved than in the other 3D reconstructions. We, therefore, performed masked 3D classification on the bound nucleic acids, which yielded a map that featured a clearly visible upstream DNA moiety (map E). Reported nominal resolution values of 3D reconstructions were calculated via RELION post-processing using the Fourier shell correlation (FSC) 0.143 cut-off criterion (Rosenthal and Henderson, 2003). Local resolution ranges were estimated using RELION.

Structural model building and refinement

Cryo-EM maps, used for structural model building, were sharpened via Local Deblur (Ramírez-Aportela et al., 2019), implemented into the Scipion software framework (de la Rosa-Trevín et al., 2016). Scipion, in turn, was run via the SBGrid software collection (Morin et al., 2013). Structural model building was performed using Coot (Casañal et al., 2020; Emsley et al., 2010). Starting models were placed into cryo-EM density maps using UCSF Chimera (Goddard et al., 2007). The first map used for structural model building was of the Pol III PTC. The model of the yeast Pol III EC (Hoffmann et al., 2015) was used as the starting model (PDB: 5FJ8). The model was first real-space refined in Coot using distance restraints to accommodate for conformational changes of the newly build model. Distance restraints were computed using ProSMART (Nicholls et al., 2012), implemented into Coot. The sequence of the DNA:RNA scaffold was mutated to resemble the scaffold used in the Pol III PTC sample. Clear additional density could be observed of the NT-strand, and the sequence of the poly-dT termination signal was manually build into this density. The model was further manually adjusted without distance restraints to fit the cryo-EM density of the Pol III PTC and real-space refined in Coot using Ramachandran restraints. The Pol III PTC model was further subjected to ISOLDE (Croll, 2018) to reduce the clash score and optimize the model geometry. For the Pol III EC structure, the Pol III PTC model was used as a starting model. Conformational changes were first adjusted by subjecting the Pol III PTC model and the Pol III EC map to the Namdinator software (Kidmose et al., 2019). The sequence of the nucleic acids was adjusted to resemble the used EC scaffold. No density of the unwound NT-strand could be observed, and the corresponding region was deleted. The Pol III EC model was further manually inspected and adjusted in Coot. For the Pol III Δ model, the procedure was the same as for the Pol III EC except that the C53/C37 heterodimer and C11 were deleted from the Pol III PTC starting model. For the Pol PTC + NTPs structure, a register shift of the DNA:RNA hybrid could be observed when inspecting the density in the active site, and the DNA:RNA hybrid was adjusted accordingly. Weak density for a nucleotide base at the position i+1 was also noticed and the 3′-end of the RNA was, therefore, extended with an adenosine monophosphate molecule. Interpretation of the upstream DNA in map E was further aided by subjecting map E to LocScale (Jakobi et al., 2017). All models were refined multiple times against the corresponding cryo-EM maps with Phenix (Liebschner et al., 2019) using Ramachandran- and secondary structure restraints. ChimeraX (Goddard et al., 2018) was used to visualize cryo-EM maps and atomic models for the structural analysis and interpretation and for figure preparation.

Residue conservation analysis

To analyze the conservation of C128 residues that contact the NT-strand, we performed a multiple-sequence alignment (MSA) of C128 orthologs from 15 eukaryotic species covering a wide range of the eukaryotic tree of life (Keeling and Burki, 2019): ophistokonts (*S. cerevisiae*, *S. pombe*, *C. elegans*, *H. sapiens*, *A. queenslandica*, *C. owczarzaki*, *S. arctica*), stramenopiles (*T. pseudonana*, *N. gaditana*); alveolata (*P. falciparum*, *T. thermophila*); archaeplastids (*P. patens*, *A. thaliana*, *C. merolae*); amoebozoans (*D. discoideum*). Next, we subjected the MSA to the Scorecons software (Valdar, 2002) to retrieve conservation scores, which were used to color-code the NT-strand-binding residues in a nucleotide-plot.

Primer extension experiments

For assembly of scaffolds used for primer extension experiments, the DNA and RNA oligonucleotides (1 μL, 20 μM each) were mixed and incubated at 95°C for 3 min. The mixture was placed immediately on ice for 1 min. Afterwards, 3 μL of 2× HB buffer were added, and the mixture was incubated at room temperature for at least 10 min. Prior to scaffold assembly, the used RNA was radioactively labelled on the 5′-end with [γ-32P]ATP (10 mCi/mL, Hartmann Analytic) and T4 PNK (NEB), following purification via PAGE. The annealed scaffold was diluted to 2 μM with transcription reaction buffer (TRB) (20 mM Hepes, pH 7.6, 60 mM $(NH_4)_2SO_4$, 10 mM MgSO4, 10% glycerol, 2 mM DTT). 1 μL of diluted scaffold was incubated with 1 μL of Pol III (4 μM, also diluted in TRB) for at least 10 min at RT. Primer extension was initiated via addition of 7 μL TRB, supplemented with NTPs (1 mM each, final concentration). The reaction was incubated at 28°C for 20 min and stopped by adding 3 μL of formamide and boiling for 4 min. The reaction was subjected to PAGE using a denaturing (8M Urea) 17% polyacrylamide TBE gel. Radioactive signal was captured with a phosphor-imaging screen (Fujifilm) and detected with a Typhon FLA9500 (GE Healthcare) instrument.

In vitro transcription experiments

Promoter-dependent and independent were performed to analyse Pol III transcription termination. Annealing of the DNA oligonucleotides (Sigma-Aldrich, desalt grade) was done similarly for the two types of experiments: 1 μL of template DNA-strand (30 μM) and

1 μL of non-template DNA-strand (30 μM) were mixed, boiled for 2 min, and immediately placed on ice for 1 min 2 μL of 2× HB (see above) were added, and the mixture was incubated at room temperature for 10 min. The annealed DNA was diluted to a concentration of 2 μM using TRB (see above) and kept on ice until usage. For promoter-independent experiments, tailed-template DNA constructs were designed to carry a single-stranded DNA overhang on the template strand. In a 5 μL reaction volume, 2 pmol of DNA were mixed with 2.5 pmol of WT or mutant Pol III, which were pre-diluted to working concentrations (0.6–2.5 μM) using EM buffer. The mixture was incubated at room temperature for 10 min, and transcription was initiated by adding 5.3 μL of a transcription initiation mix (3.9 μL of TRB, 0.7 μL NTP mix (10 mM ATP, 10 mM CTP, 1 mM UTP) and 0.7 μL of [α-P32]UTP (10 mCi/mL)). The reactions were incubated at room temperature for 40 min. Afterwards, 138 μL of stop buffer (0.6 M NaAcetate, 30 mM EDTA, 0.5% SDS) were added, and the reaction was subjected to phenol-chloroform extraction, boiling for 3 min, and denaturing PAGE using a 15% polyacrylamide TBE-Urea gel. Radioactive signal was recorded as described above. For promoter-dependent transcription assays, a double-stranded (ds) DNA hybrid construct was designed that consisted of the *S. cerevisiae* U6 snRNA promoter region and a portion of the *S. cerevisiae* tDNA gene tL(CAA)L featuring a 5-dT termination signal. Nucleic acids were annealed as described above. Pol III was diluted to 5 μM using TRB. Yeast TFIIIB, which was used to recruit Pol III to the promoter region, was freshly assembled by mixing a fusion construct of Brf1 and TBP (Brf1-TBP) with Bdp1, which were expressed and purified as described in (Vorländer et al., 2018). TFIIIB was assembled by mixing 2.4 μL of Bdp1 (6 mg/mL), 2.8 μL of Brf1-TBP (6 mg/mL) and 4.8 μL of TRB-300 (20 mM Hepes, pH 7.6, 300 mM NaCl, 60 mM $(NH_4)_2SO_4$, 10 mM $MgSO_4$, 10% glycerol, 2 mM DTT). The mixture was incubated on ice for 10 min and diluted to 5 μM using TRB-300. Next, 5 pmol of assembled TBIIIB were incubated with 2.5 pmol of dsDNA on ice for 10 min. Subsequently, 5 pmol of Pol III were added and the mixture was incubated for at least 10 min on ice. Transcription was initiated by adding 5.4 μL of transcription initiation mix (3.9 μL of TRB, 0.7 μL NTP mix (10 mM ATP, 10 mM CTP, 10 mM GTP, 1 mM UTP) and 0.7 μL of [α-P32]UTP (10 mCi/mL)). The reaction was incubated at 28 °C. Typically, time courses were performed by stopping the reaction at the desired time points with 4 μL formamide loading buffer and boiling at 3 min. The reactions were directly loaded on 15% denaturing PAGE and radioactive transcription products were recorded as described above. The here-shown gels derived from promoter-dependent transcription experiments were not performed in triplicates but the reproducibility could be confirmed by performing the experiments multiple times for different analytical purposes.

Mutagenesis of *S. cerevisiae* C128 for structure-function studies

CRISPR-Cas9-mediated genome engineering was used for site-directed mutagenesis of the endogenous *S. cerevisiae* C128-coding gene (*RET1*). A C128-TAP-tagged yeast strain (Euroscarf ID: SC2330) was used for genome engineering. Guide RNAs (sgRNA) were designed using the Benchling CRISPR Guide RNA Design tool (2021), retrieved from https://benchling.com, and ordered as DNA oligonucleotides in forward and reverse directions. For cloning of the sgRNA constructs, the oligonucleotides were phosphorylated via T4 PNK (NEB), mixed, and annealed by incubating the mixture at 95°C for 6 min and letting it cooling down to room temperature. Next, 2 μL of the annealed dsDNA was mixed with 0.5 μL of the pWS082 entry vector (which was a gift from Tom Ellis lab and Addgene plasmid # 90516) (at a concentration of 200–300 ng/uL), 1 μL each of T4 ligase, 10× T4 ligase buffer, and BmsbI. In a thermocycler, the mixture was incubated at 42°C (2 min) and 16°C (5 min), and the cycle was repeated 10 times. Next, the reaction was incubated at 60°C for 10 min and lastly at 80°C for 10 min. The reaction was transformed into *E. coli* XL-1 Blue chemically competent cells (Agilent). The next day, positive clones were selected by using a Typhoon imager with a GFP-filter to screen for GFP-negative colonies. DNA donor constructs (containing the mutated DNA sequence to generate the corresponding C128 mutation) were designed to contain 50 base pairs (bps) homology arms at either side of the desired DNA break. The oligonucleotides were ordered as two partially complementary (20 bps) primers in forward and reverse direction, amplified via polymerase chain reaction (PCR), and purified via ethanol precipitation. The Cas9-sgRNA gap repair vector pWS174 (which was a gift from Tom Ellis lab and Addgene plasmid # 90961) was linearized with BsmBI (NEB) and gel-purified. The cloned sgRNA entry vectors were digested with EcoRV. For transformation into yeast cells, 5 μg of dsDNA donor DNA, 100 ng of linearized pWS174, and 200 ng of linearized sgRNA entry vector were mixed and transformed into yeast cells via the lithium acetate (LiAc)/sorbitol method. 50 mL of yeast cells at an $OD_{600\ nm}$ of 0.6 were spun down (2500 rpm, 5 min RT), washed once with a mix of LiAc (1M)/Sorbitol (1M) and resuspended in 600 μL LiAC/Sorbitol. The DNA mixture (above) was added to 100 μL of the yeast LiAc/Sorbitol suspension, and the mixture was added to a pre-mix containing 280 μL of 50% PEG 4000 and 15 μL sperm carrier DNA. The reaction was incubated at RT for 1 h, 40 μL of DMSO were added, and the reaction was incubated at 42°C for 20 min while slowly shaking. Next, 1 mL of YPD were added, followed by centrifugation (3000 rpm, 2 min). The pellet was dissolved in 500 μL YPD, transferred into 15 mL tubes containing 4.5 mL YPD, and the mixture was incubated at 30°C for a least 3 h. The cell suspension was spun at 2300 rpm for 5 min, dissolved in 500 μL PBS, spread on YPD plates supplemented with Nourseothricin (clonNAT) (100 ug/mL), and kept at 30°C. After three days, yeast colonies were re-streaked on YPD plates without clonNAT and incubated for another two or three days. Positive clones (those who contain the desired mutation) were screened via colony PCR and subsequent Sanger sequencing.

Yeast spotting assays

YPD medium was inoculated with yeast cultures, and the yeast starter cultures were grown over night at 30°C shaking. The next day, the $OD_{600\ nm}$ was measured, the cultures were diluted to an $OD_{600\ nm}$ of 0.2 using fresh YPD, and the cultures were incubated for another 4 h. Next, the cultures were diluted to $OD_{600\ nm}$ = 0.2 using PBS. The PBD-diluted cell suspensions were used to make

10-fold serial dilutions in PBS (3 steps). Starting with the $OD_{600\ nm}$ 0.2 dilutions, the diluted cultures were applied onto YPAD plates as single 8 μL drops. The plates were incubated at 25, 30 or and 37°C and imaged after 3 days.

UV crosslinking and analysis of cDNA (CRAC)

CRAC was performed using Pol III C128 WT and mutants yeast strains that carried an HTP-tag on subunit C160. The TAP-tag of C128 was, thus, removed for all three tested mutant yeast strains and replaced with a HTP-tag on C160 via homologous recombination. The CRAC protocol used in this study is derived from (Granneman et al., 2009) and modified as previously described (Candelli et al., 2018). Briefly, 2 L of yeast cells expressing an HTP-tagged version of C160 were grown at 30°C to $OD_{600\ nm}$ 0.4–0.6 in CSM-TRP medium. Cells were crosslinked for 50 s using a W5 UV crosslinking unit (UVO3 Ltd) and harvested by centrifugation. Cell pellets were washed once with cold 1xPBS and resuspended in 2.4 mL/(g of cells) TN150 buffer (50 mM Tris pH 7.8, 150 mM NaCl, 0.1% NP-40 and 5 mM β-mercaptoethanol) in the presence of protease inhibitors (Complete™ EDTA-free Protease Inhibitor Cocktail, Roche). Suspensions were flash frozen in droplets and cells subjected to cryogenic grinding using a Ball Mill MM 400 (5 cycles of 3 min at 20 Hz). The resulting frozen cell lysates were thawed on ice, digested with DNase I (165 units per gram of cells) at 25°C for 1h, and then clarified by centrifugation at 13,000 rpm for 30 min at 4°C. Protein extracts were quantified by Bradford reagent (Sigmal) and the same amount of extracts for each sample were subjected to IgG affinity purification as described below.

RNA-protein complexes were bound on M-280 tosylactivated dynabeads coupled with rabbit IgGs (10 mg of beads per sample), washed with TN1000 buffer (50 mM Tris pH 7.8, 1 M NaCl, 0.1% NP-40 and 5 mM β-mercaptoethanol), and eluted by TEV protease digestion. RNAs in the eluates were shortened by treating with 0.2 U of RNase cocktail (RNace-IT, Agilent) and the reaction was stopped by adding of guanidine–HCl to a final concentration of 6 M. The eluates were then incubated with Ni-NTA sepharose (Qiagen, 100 μL of slurry per sample) at 4°C overnight and extensively washed. Sequencing adaptors were ligated to the RNA molecules as described in Granneman et al. (2009). RNA-protein complexes were recovered with elution buffer (50 mM Tris pH 7.8, 50 mM NaCl, 150 mM imidazole, 0.1% NP-40 and 5 mM β-mercaptoethanol) and fractionated by Gel Elution Liquid Fraction Entrapment Electrophoresis (GelFree) system (Expedeon) according to manufacturer's instructions. The fractions containing Rpc160 were digested with 100 μg of proteinase K, and RNAs were purified and reverse-transcribed using reverse transcriptase Superscript IV (Invitrogen).

The resulting cDNAs were amplified by PCR using LA Taq polymerase (Takara), and the PCR reactions were then treated with 200 U/mL of Exonuclease I (NEB) for 1 h at 37°C. The final library was purified using NucleoSpin columns (Macherey-Nagel) and sequenced on a NextSeq 500 Illumina sequencer.

QUANTIFICATION AND STATISTICAL ANALYSIS

Cryo-EM data were processed with RELION and cryoSPARC. Structural models were refined with Phenix. The corresponding statistics can be found in Table S1 and Data S1–S4.

For quantification and analysis of *in vitro* transcription experiments, RNA band intensities were quantified via the Image Lab software (Bio-Rad). Bar plots were generated in R. To normalize the radioactive signals of the bands of interest, their band intensities were divided by total lane intensities that contained the respective band of interest. The calculated values were multiplied by a factor of thousand for illustrative purposes. Tailed-template experiments were performed in triplicates (N = 3, technical replicates), except for the mutant K448A on the 3-dT construct, which was done in duplicates (N = 2, technical replicates). Mean values and standard deviations were calculated in R.

For CRAC experiments, two technical replicates were performed and were processed and statistically analysed as follows:

For CRAC data processing, the sequencing dataset was processed as described in (Xie et al., 2022) with some modification. Briefly, CRAC reads were demultiplexed using the pyBarcodeFilter script from the pyCRACutility suite (Webb et al., 2014). The 5′ adaptor was clipped with Cutadapt and the resulting insert quality-trimmed from the 3′ end using Trimmomatic rolling mean clipping (Bolger et al., 2014). PCR duplicates were collapsed by the pyCRAC script pyFastqDuplicateRemover using a 6-nucleotide random tag included in the 3′ adaptor. The resulting sequences were reverse complemented with the Fastx reverse complement that is included in the fastx toolkit (http://hannonlab.cshl.edu/fastx_toolkit/) and mapped to the R64 genome with bowtie2 using "-N 1" option. Reads shorter than 20 nt were filtered out after mapping. Reads mapped to 37S rDNA unit (transcribed by Pol I) were also excluded from analysis to reduce the background signals. Reads mapping to multiple sites (e.g. most reads mapping to mature tRNA regions) were attributed randomly to one of the matching sites. Coverage bigwig files were generated and normalized to counts per million (CPM) using the bamCoverage tool from the deepTools package (Ramírez et al., 2016) using a bin size of 1.

For bioinformatic analysis, yeast genome was obtained from Saccharomyces Genome Database (*S. cerevisiae* genome version R64-2-1). tRNA coordinate files (from 5′ end to the end of the primary terminator) were obtained from (Xie et al., 2022). For each tRNA gene, the primary terminator was defined as the 1st T-tract after the 3′ end of the mature tRNA. Four pairs of tRNAs that are arranged in tandem were excluded from the following analysis.

Reads mapped to different classes of RNAs were summarized by BEDTools coverage. Coverage files were analyzed with deepTools suite (Ramírez et al., 2016). Specifically, for metagene analysis of Pol III occupancy, strand-specific bigwig files and tRNA coordinate files were used as inputs for the computeMatrix tool using a bin size of 1 and the scale-regions mode. The matrices generated were then combined by the computeMatrixOperations tool with the rbind option and used as inputs for the plotProfile tool. For heatmap analyses, the log2 ratio of the Pol III signal in the indicated mutants relative to the WT was calculated by the bigwigCompare

tool using a bin size of 1, and the resulting files were used as inputs for the computeMatrix as described above. The final matrix after combination was used as inputs for the plotHeatmap tool. To analyze the correlation between two replicates, the average Pol III signal over regions comprising tRNA genes and 500 bp upstream and downstream regions was computed using the multiBigwigSummary tool. The signals calculated were then compared by plotCorrelation tool to generate scatter plots and compute the correlation coefficients using the Spearman method.

The efficiency of transcription termination in the WT and the mutants was estimated by calculating the read-through index (RT index) defined as the percentage of Pol III signal over the read-through regions (500 bp region immediately downstream of the primary terminator of each tRNA gene) relative to the signal over tRNA gene regions (from 5' end to the end of the primary terminator). The total Pol III signal at each region was computed with the UCSC bigWigAverageOverBed package (http://genome.ucsc.edu).

Data representation and statistical analyses were performed with R using the ggpubr (https://rpkgs.datanovia.com/ggpubr/) and dplyr (https://dplyr.tidyverse.org/) packages.

Cell Reports, Volume *40*

Supplemental information

Architecture of the yeast Pol III pre-termination complex and pausing mechanism on poly(dT) termination signals

Mathias Girbig, Juanjuan Xie, Helga Grötsch, Domenico Libri, Odil Porrua, and Christoph W. Müller

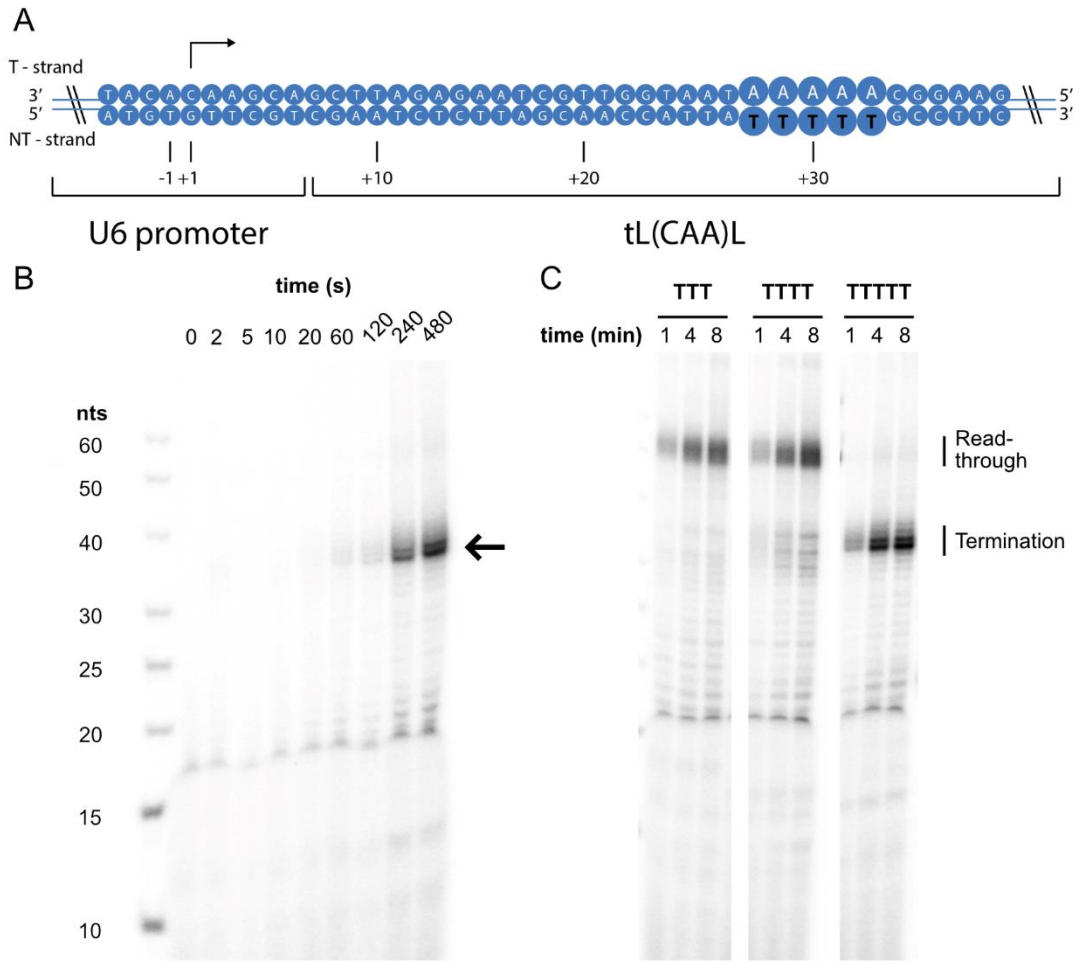

Figure S1. Pol III terminates transcription on poly-dT sequences *in vitro*, Related to Figure 1.

(A) Schematic of the *S. cerevisiae* dsDNA construct, containing the U6 snRNA promoter and the 3'-flanking site of the L(CAA)LR2 gene. The construct was used for promoter-dependent transcription experiments. The termination signal is highlighted in bold letters.

(B) Denaturing RNA gel of the promoter-dependent transcription experiment. Shown is a time course of probes taken at the indicated time points. A radioactive RNA product becomes visible over time that is labelled with an arrow; n (dsDNA) = 2.5 pmol; n (Pol III) = 5 pmol; n (TFIIIB) = 5 pmol. 15% TBE denaturing PAGE. The gels were cropped for clarity.

(C) Time-course of the Pol III transcription experiment testing the effect of a 5-dT, 4-dT, or 3-dT sequence on Pol III transcription termination. Same conditions as in (B). The gel has been cropped for clarity.

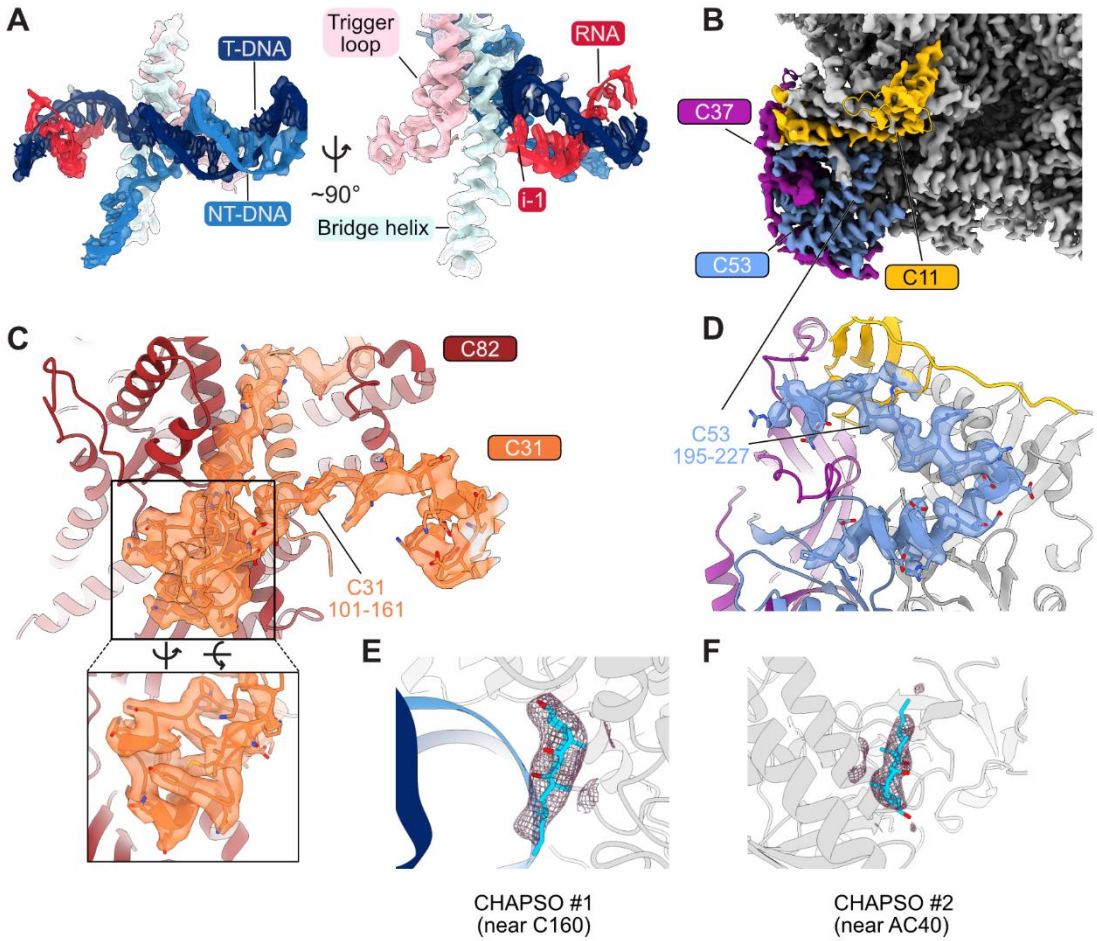

Figure S2. Cryo-EM data quality of the active site elements and newly build regions, Related to Figure 1.

(A) Close-up views on the Pol III PTC active site elements. Cryo-EM densities are shown as transparent surfaces.

(B) The C11 C-terminal domain is visible and binds the Pol III core close to the C160 jaw domain and subunit ABC27.

(C) Newly built region (101-161) of the Pol III heterotrimer subunit C31. Cryo-EM density of the newly assigned region is shown as a transparent surface.

(D) Newly built region (195-227) of the Pol III heterodimer subunit C53. Cryo-EM density of the newly assigned region is shown as a transparent surface.

(E) - (F) Cryo-EM densities of putative CHAPSO molecules, of which the tetracyclic sterol head groups were placed.

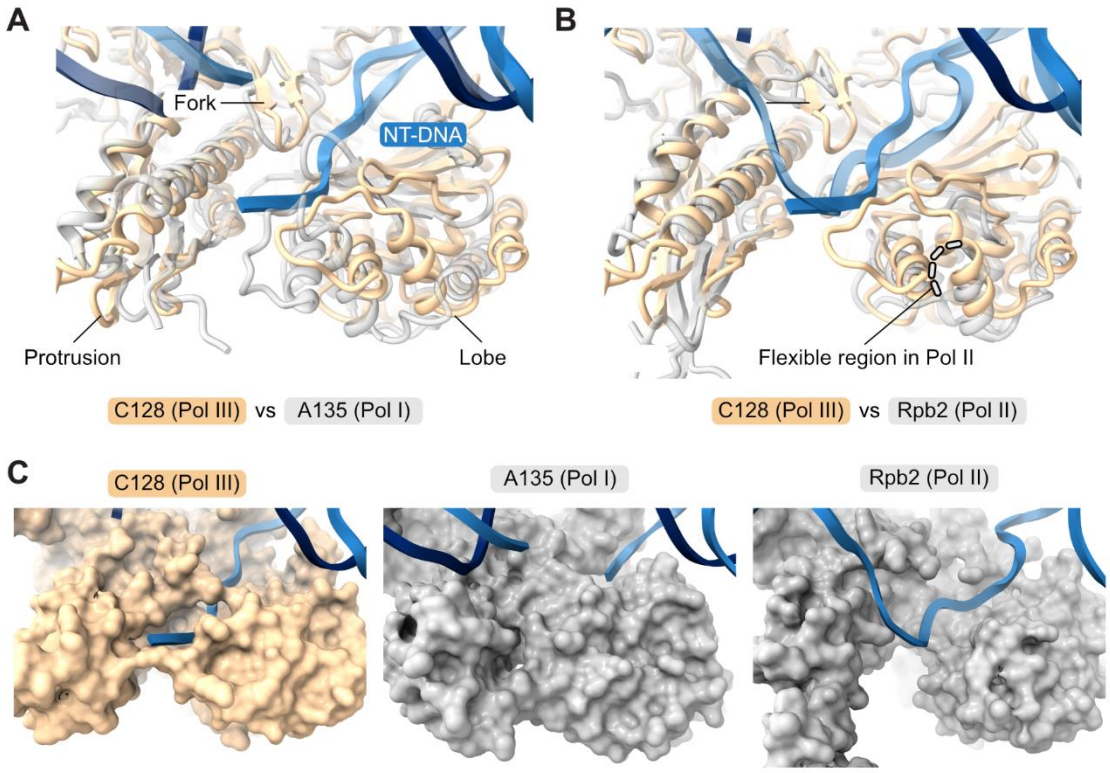

Figure S3. NT-strand exit channel comparison between yeast Pol III PTC and yeast Pol I and Pol II EC structures, Related to Figures 1, 2.

(A) Superimposition of the Pol III PTC and the Pol I EC (PDB: 6HLR). The C128 fork, protrusion, and lobe domains are labelled.

(B) Superimposition of the Pol III PTC and the Pol II EC (PDB: 5C4J).

(C) Calculated surface representations of C128 (Pol III PTC, left), A135 (Pol I EC, middle), and Rpb2 (Pol II EC, right).

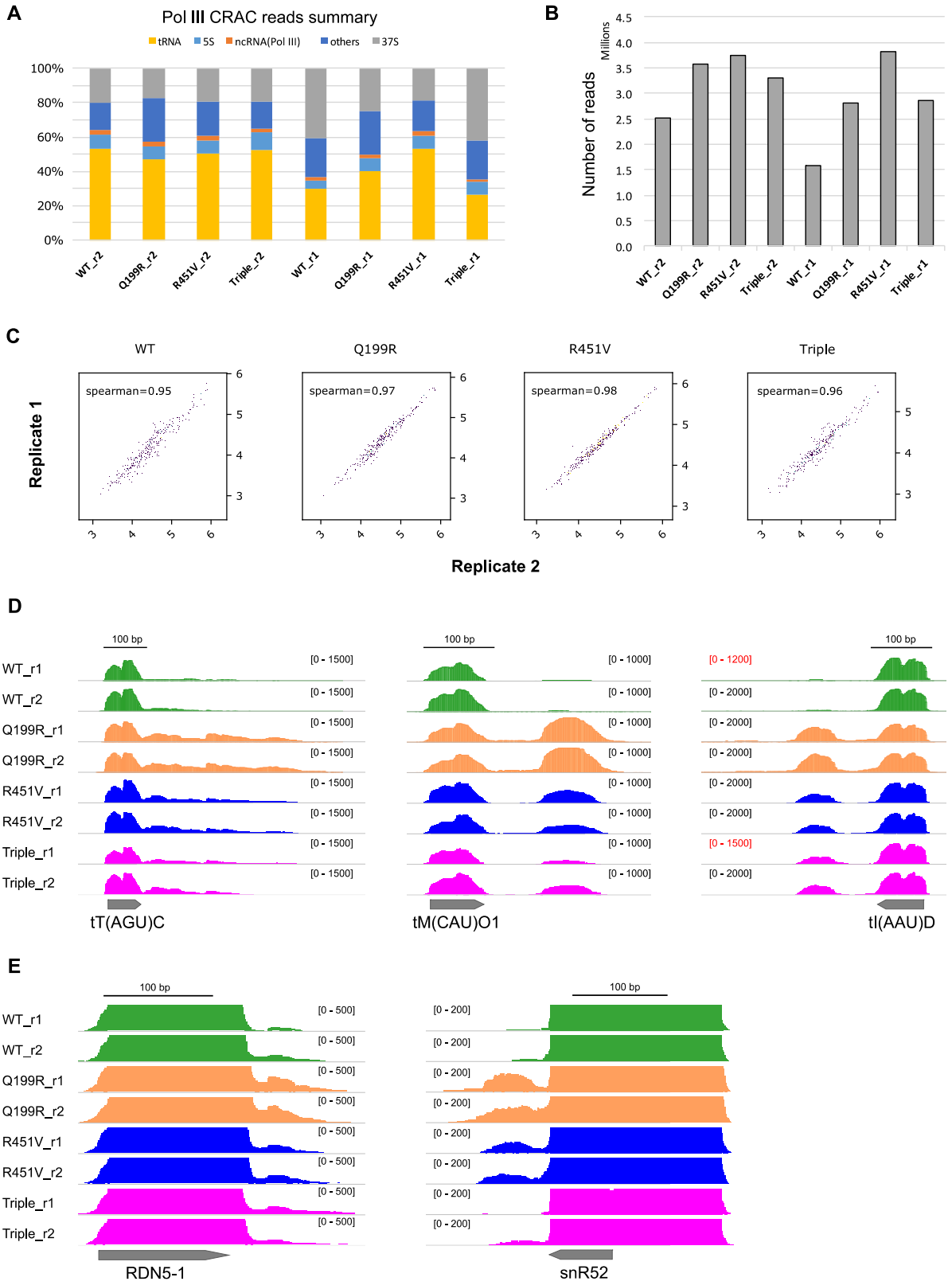

Figure S4. Complementary analyses validating CRAC experiments, Related to Figure 4.

A) Comparison of the read distribution among different genomic regions in the indicated strains in our Pol III CRAC experiment. The "others" category corresponds to Pol II genes and intergenic regions. Note that we have more contaminants and lower signal at tRNA regions in the WT_r1 and Triple_r1

samples, which, however, does not significantly affect the assessment of the transcription termination efficiency.

B) Plot representing the number of mapped reads obtained in a typical CRAC experiment in the different samples. "M" denotes millions.

C) Scatter plots showing the high correlation, calculated by the Spearman method, between the two biological replicates of each strain for the CRAC experiments showed in figure 4.

D) Integrative Genomics Viewer (IGV) screenshots of examples of tRNA genes displaying termination defects in the two biological replicates of each strain. The values under brackets correspond to the scale of the Pol III signal expressed in CPM. Note that because of the higher amounts of contaminants in the WT_r1 and Triple_r1 samples, the signal in the tRNA regions is lower (scale indicated in red), but the Pol III distribution is similar as in the other replicate of the same strains (r2).

E) IGV screenshots of RNAPIII-dependent genes other than tRNA genes presenting termination defects in RNAPIII mutants. Images are zoom in views of the corresponding termination regions.

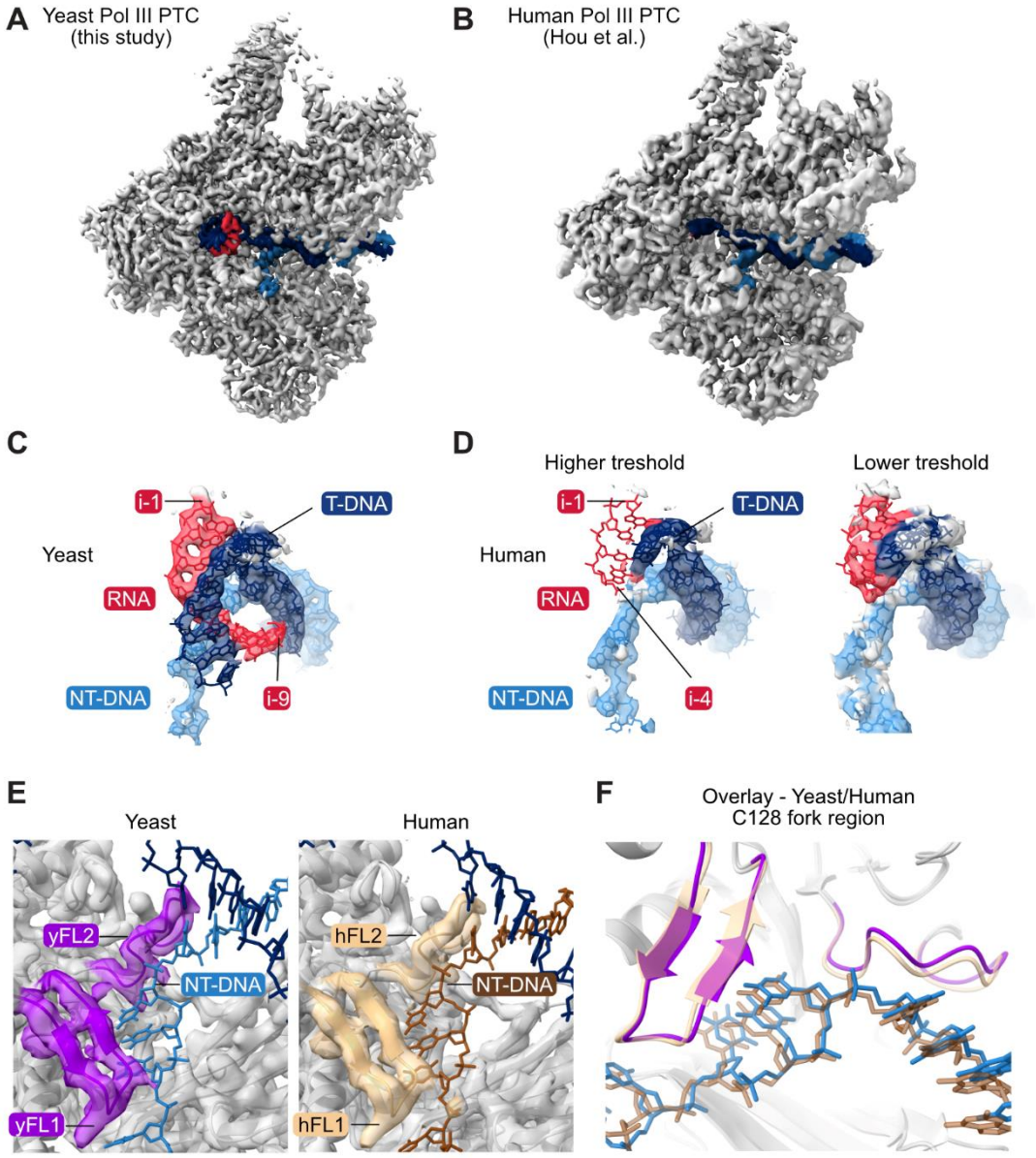

Figure S5. Comparison between yeast and human Pol III PTC, Related to Figures 1, 2.

(A) Cryo-EM map (unsharpened) of the yeast Pol III PTC (map A). Colour scheme: Pol III – grey, RNA – red, template (T)-DNA – dark blue, non-template (NT)-DNA – light blue.

(B) Cryo-EM map of the human Pol III PTC (EMD-31622; Hou et al., 2021). Colour scheme as in (A).

(C) Close-up view onto the active site of the yeast Pol III PTC (map A, unsharpened). Nucleic acid elements are coloured as in (A) and are labelled, accordingly. The 'i-1' refers to the nucleotide position adjacent to the nucleotide (i) addition site and marks the 3'-end of the RNA. 'i-9' marks the last RNA base that could build with high confidence. Threshold level is similar as in (A).

(D) Close-up view onto the active site of the human Pol III PTC (EMD-31622; Hou et al., 2021). Nucleic acid elements are coloured as in (C). Shown is the supplementary (derived from focused refinement onto the Pol III core) cryo-EM map of EMD-31622. Cryo-EM densities are shown at two

threshold levels (left one is similar as in (B)) to illustrate that the RNA in the human Pol III PTC is only weekly bound and can only be observed at lower cryo-EM threshold levels.

(E) Close-up views onto the fork regions of the yeast (y) (left) and human (h) (right) PTC structures and corresponding cryo-EM maps (in grey). The fork loop (FL) 1 and 2 elements (yeast – purple, human – burly-wood) and the NT-strands (yeast – light blue, human – brown) are coloured and labelled. Only subunits C128 (yeast) and RPC2 (human) are shown.

(F) Close-up view onto the Pol III fork region and overlay between atomic models of the yeast (solid ribbon model) and human Pol III (transparent ribbon model) PTC. Models are coloured as in (E).

Table S1. Cryo-EM data collection, refinement and validation statistics, Related to Figures 1, 2, 5, 6 and Data S1-S4

	Pol III PTC Map A	**Pol III EC Map B**	**Pol III Δ Map C**	**Pol III PTC + NTPs Map D**	**Pol III PTC + NTPs 2 Map E**
PDB code	7Z1L	7Z1M	7Z1N	7Z1O	-
EMDB code	EMD-14447	EMD-14448	EMD-14449	EMD-14451	EMD-14450
Data collection and processing					
Magnification	130,000	130,000	81,000	130,000	130,000
Voltage (kV)	300	300	300	300	300
Electron exposure (e–/Å^2)	40.9	38.1	39.6	44.8	44.8
Defocus range (μm)	0.75-2.25	0.50-1.75	1.00-2.50	0.75-2.25	0.75-2.25
Pixel size (Å)	1.041	1.040	1.053	1.041	1.041
Symmetry imposed	C1	C1	C1	C1	C1
Initial particle images (no.)	464,321	248,884	359,678	538,161	538,161
Final particle images (no.)	47,222	24,295	18,530	237,468	23,641
Map resolution (Å)	2.8	3.4	3.9	2.7	3.2
FSC threshold	0.143	0.143	0.143	0.143	0.143
Map resolution range (Å)	2.5-8.0	3.2-8.8	3.7-8.5	2.5-5.1	2.9-7.5
Refinement					
Initial model used (PDB code)	6TUT, 5FJ8, 5FJA	6TUT, 5FJ8, 5FJA	6TUT, 5FJ8, 5FJA	6TUT, 5FJ8, 5FJA	
Model resolution (Å)	3.0	3.4	3.9	3.0	
FSC threshold	0.5	0.5	0.5	0.5	
Map sharpening *B* factor (Å^2)	-27.6	-70.4	-107.1	-66.4	
Model composition					
Non-hydrogen atoms	42,330	42,127	38,605	42,375	
Protein/nucleotide residues	5156/63	5153/53	4705/56	5154/66	
Ligands	5x Zn, 1x Mg, 2x 1N7	5x Zn, 1x Mg, 2x 1N7	5x Zn, 1x Mg, 2x 1N7	5x Zn, 1x Mg, 2x 1N7	
B factors (Å^2)					
Protein	73.63	112.52	56.95	61.03	
Nucleotide	90.42	157.39	84.51	79.65	
Ligand	73.44	116.06	61.34	67.07	
R.m.s. deviations					
Bond lengths (Å)	0.003	0.004	0.005	0.003	
Bond angles (°)	0.636	0.678	0.779	0.640	
Validation					
MolProbity score	1.34	1.45	1.68	1.28	
Clashscore	4.14	4.73	6.26	3.96	
Poor rotamers (%)	0.02	0.00	0.00	0.00	
Ramachandran plot					
Favored (%)	97.23	96.68	95.13	97.55	
Allowed (%)	2.77	3.30	4.83	2.45	
Disallowed (%)	0.00	0.02	0.04	0.00	

Table S2. Used oligonucleotides, Related to Key Resource Table.

Name and usage	Source	Sequence (5' to 3')
Template strand for scaffolds SC1 and SC2, used for RNA primer extension assays and cryo-EM sample prep (Pol III PTC)	This paper	CAAAATTTTCGGAAGGCATGCTCTGTGGCTTTGCTAAGAGATTC
Scaffold 1 (SC1), used for RNA primer extension assays and cryo-EM sample prep (Pol III PTC), non-template strand	This paper	GAATCTCTTAGCAACCATTATTTTTTTGCCTTCCGAAAATTTTG
Scaffold 2 (SC2), used for RNA primer extension assays and cryo-EM sample prep (Pol III EC), non-template strand	This paper	GAATCTCTTAGCAACCATTAGCTTGCTGCCTTCCGAAAATTTTG
Template strand for promoter-dependent transcription assay, 5 dT-termination site	This paper	CAAAATTTTCGGAAGGCAAAAATAATGGTTGCTAAGAGATTCGACGAACACATAGTTGCGAAAAAAACATTTTTTTATAGTAGCCGAAAATAG
Non-template strand for promoter-dependent transcription assay, 5 dT-termination site	This paper	CTATTTTCGGCTACTATAAAAAAATGTTTTTTTCGCAACTATGTGTTCGTCGAATCTCTTAGCAACCATTA**TTTTT**GCCTTCCGAAAATTTTG
Template strand for promoter-dependent transcription assay, 4 dT-termination site	This paper	TCAAAATTTTCGGAAGGCAAAATAATGGTTGCTAAGAGATTCGACGAACACATAGTTGCGAAAAAAACATTTTTTTATAGTAGCCGAAAATAG
Non-template strand for promoter-dependent transcription assay, 4 dT-termination site	This paper	CTATTTTCGGCTACTATAAAAAAATGTTTTTTTCGCAACTATGTGTTCGTCGAATCTCTTAGCAACCATTA**TTTT**GCCTTCCGAAAATTTTGA
Template strand for promoter-dependent transcription assay, 3 dT-termination site	This paper	TTCAAAATTTTCGGAAGGCAAATAATGGTTGCTAAGAGATTCGACGAACACATAGTTGCGAAAAAAACATTTTTTTATAGTAGCCGAAAATAG
Non-template strand for promoter-dependent transcription assay, 3 dT-termination site	This paper	CTATTTTCGGCTACTATAAAAAAATGTTTTTTTCGCAACTATGTGTTCGTCGAATCTCTTAGCAACCATTA**TTT**GCCTTCCGAAAATTTTGAA
Template strand for tailed-template transcription assay, 6 dT-termination site	This paper	GTTGGTAGTGGCGGTTGTAGGAAAAAAGATTGGAATTAGGTGGATGAGAGGGGTTATG
Non-template strand for tailed-template transcription assay, 6 dT-termination site	This paper	CCACCTAATTCCAATC**TTTTTT**CCTACAACCGCCACTACCAAC
Template strand for tailed-template transcription assay, 3 dT-termination site	This paper	GTTGGTAGTGGcGGTTGTAGGGTGAAAGATTGGAATTAGGTGGATGAGAGGGGTTATG
Non-template strand for tailed-template transcription assay, 3 dT-termination site	This paper	CCACCTAATTCCAATC**TTT**CACCCTACAACCgCCACTACCAAC
CRISPR-Cas9 donor, C128 Triple mutant, forward	This paper	CCAGACTATCTTATATTTCCGCATTGGGTATGATGACAAGAATTTCTTCTGCcTTTGAAGCtTCAGGtAAA

CRISPR-Cas9 donor, C128 Triple mutant, reverse	This paper	CAGTACAAAGCATACCAAATT GAGAAGGTTGTAATGCTCTTG GACCGGAAACTTTACCTGAAG CTTCAAAGG
CRISPR-Cas9 donor, C128 Q199R mutant, forward	This paper	GTGGTTACTTTATTGTTAACG GTACCGAAAAAGTAATTCTTG TTCAAGAAagaTTATCaAAGAA TCGTAT
CRISPR-Cas9 donor, C128 Q199R mutant, reverse	This paper	GGAGGCCTGAACAATGCCTTT CTTCTCATCTGCCTCCACAAT AATACGATTCTTtGATAAtctTTC T
CRISPR-Cas9 donor, C128 R451V mutant, forward	This paper	TGAACAGAGCTATCTCAACCG GTAATTGGTCTCTTAAAAGATT TAAGATGGAAGTTGCGGGTGT T
CRISPR-Cas9 donor, C128 R451V mutant, reverse	This paper	CATACCCAATGCGGAAATATA AGATAGTCTGGAAAGAACATG TGTAACACCCGCAACTTCCAT CT
CRISPR-Cas9 donor, C128 K448A mutant, forward	This paper	GCGGACTGAACAGAGCTATCT CAACCGGTAATTGGTCTCTTA AAAGATTTgctATGGAgAGGGC G
CRISPR-Cas9 donor, C128 K448A mutant, reverse: 5'- -3'	This paper	CCCAATGCGGAAATATAAGAT AGTCTGGAAAGAACATGTGTA ACACCCGCCCTcTCCATagcAA ATC
CRISPR-Cas9 donor, C128 R481 mutant	This paper	TTATATTTCCGCATTGGGTATG ATGACAAGAATTTCTTCTCAGT TTGAAAAATCAGGTAAAGTTTC CGG
CRISPR-Cas9 donor, C128 R481 mutant	This paper	ATCTGCAGTACAAAGCATACC AAATTGAGAAGGTTGTAATGC TCTTGGACCGGAAACTTTACC TGATTT
CRISPR-Cas9 donor, C128 H225 mutant, forward	This paper	GTGGAGGCAGATGAGAAGAA AGGCATTGTTCAGGCCTCCGT TACTTCATCTACCCTTGAAAGA AAAT
CRISPR-Cas9 donor, C128 H225 mutant, reverse	This paper	TGCTTCAAATAGATCTTGCCAT TTTTGGTAATGACATAAGTCTT AGATTTTCTTTCAAGGGTAGAT
CRISPR-Cas9 donor, C128 R451-to-WT, forward	This paper	TGAACAGAGCTATCTCAACCG GTAATTGGTCTCTTAAAAGATT TAAGATGGAAAGAGCGGGTGT T
CRISPR-Cas9 donor, C128 R451-to-WT mutant, reverse	This paper	CATACCCAATGCGGAAATATA AGATAGTCTGGAAAGAACATG TGTAACACCCGCTCTTTCCAT CT

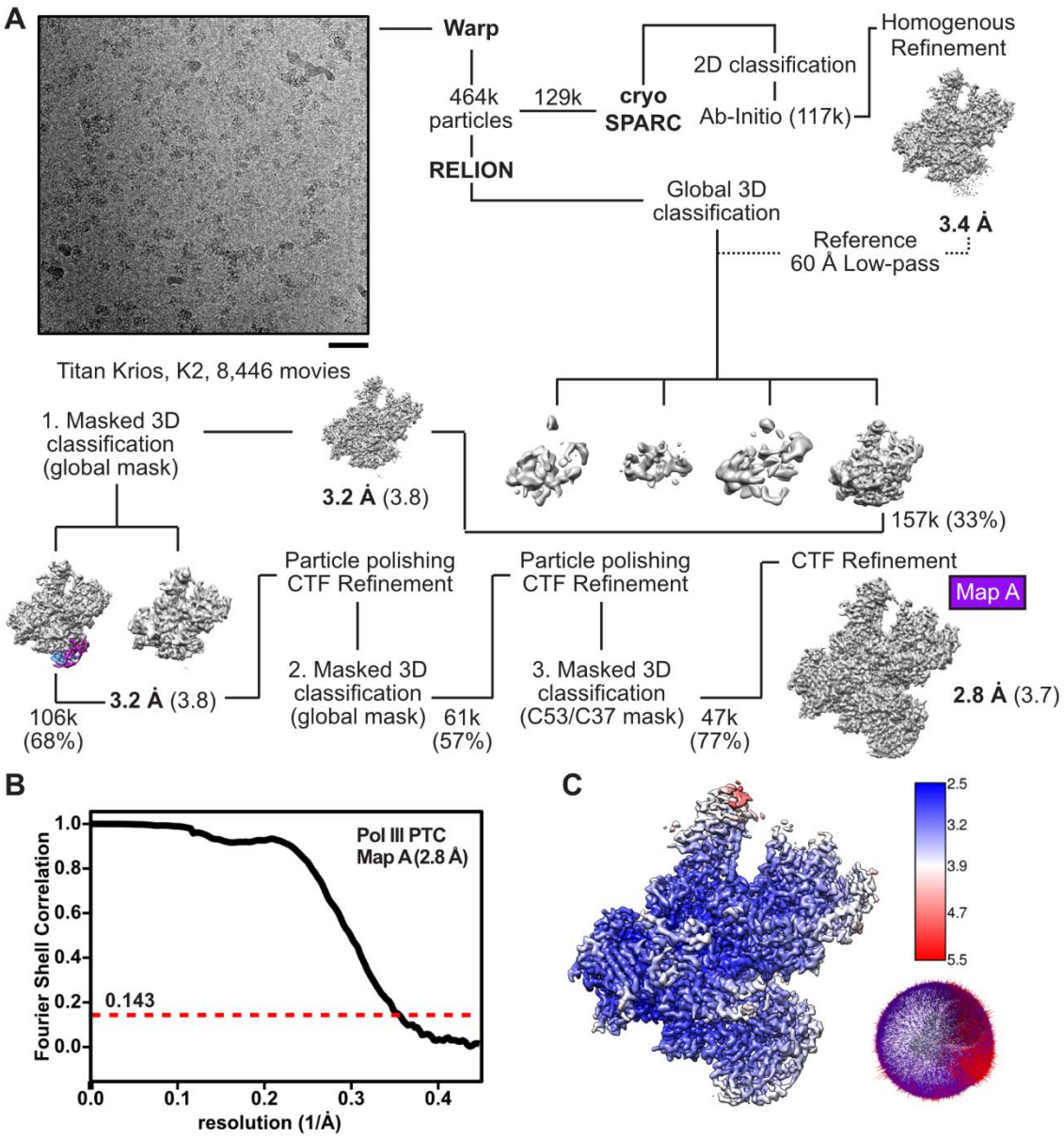

Data S1. Data-collection and -processing workflow of the yeast Pol III PTC, Related to Figure 1.

(A) Cryo-EM data collection and processing strategy for the yeast Pol III PTC. Particle numbers are rounded down. Shown are the unsharpened cryo-EM maps obtain via 3D refinement in RELION. Reported resolution values are given below the cryo-EM maps and correspond to sharpened maps obtained via RELION post-processing. The resolution values of the unsharpened 3D maps are added in round brackets. Map features that show improved cryo-EM signal after masked 3D classification are highlighted in colours. Scale bar: 50 nm.

(B) Fourier shell correlation (FSC) curve of the yeast Pol III PTC derived via RELION post-processing (FSC = 0.143).

(C) Estimation of local resolution and angular distribution plot of the yeast Pol III PTC. Shown is the unsharpened cryo-EM map.

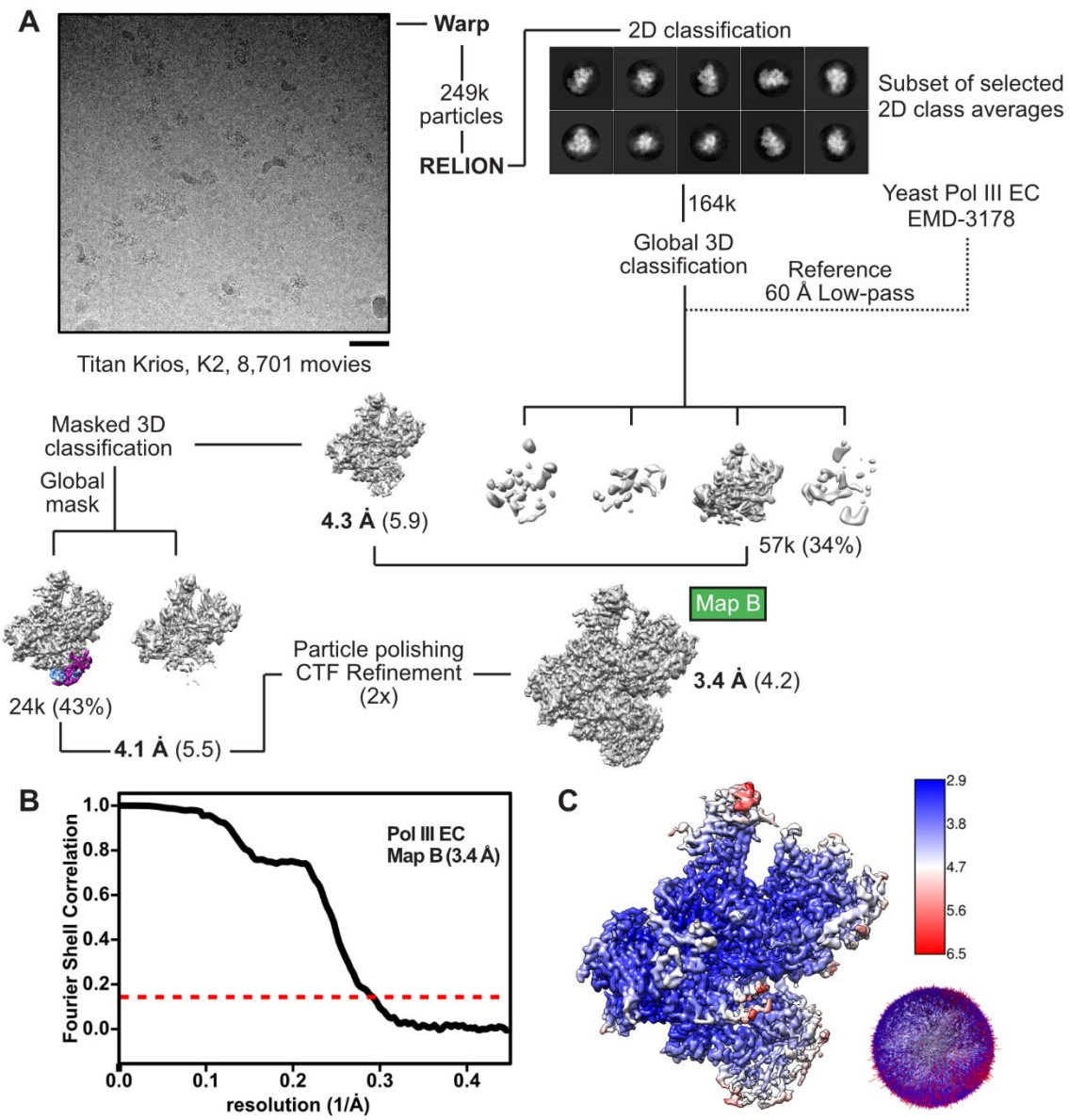

Data S2. Data-collection and -processing workflow of the yeast Pol III EC, Related to Figure 1.

(A) Cryo-EM data collection and processing strategy for the yeast Pol III EC. Particle numbers are rounded down. Shown are the unsharpened cryo-EM maps obtain via 3D refinement in RELION. Reported resolution values are given below the cryo-EM maps and correspond to sharpened maps obtained via RELION post-processing. The resolution values of the unsharpened 3D maps are added in round brackets. Map features that show improved cryo-EM signal after masked 3D classification are highlighted in colours. Scale bar: 50 nm.

(B) Fourier shell correlation (FSC) curve of the yeast Pol III EC derived via RELION post-processing (FSC = 0.143).

(C) Estimation of local resolution and angular distribution plot of the yeast Pol III EC. Shown is the unsharpened cryo-EM map.

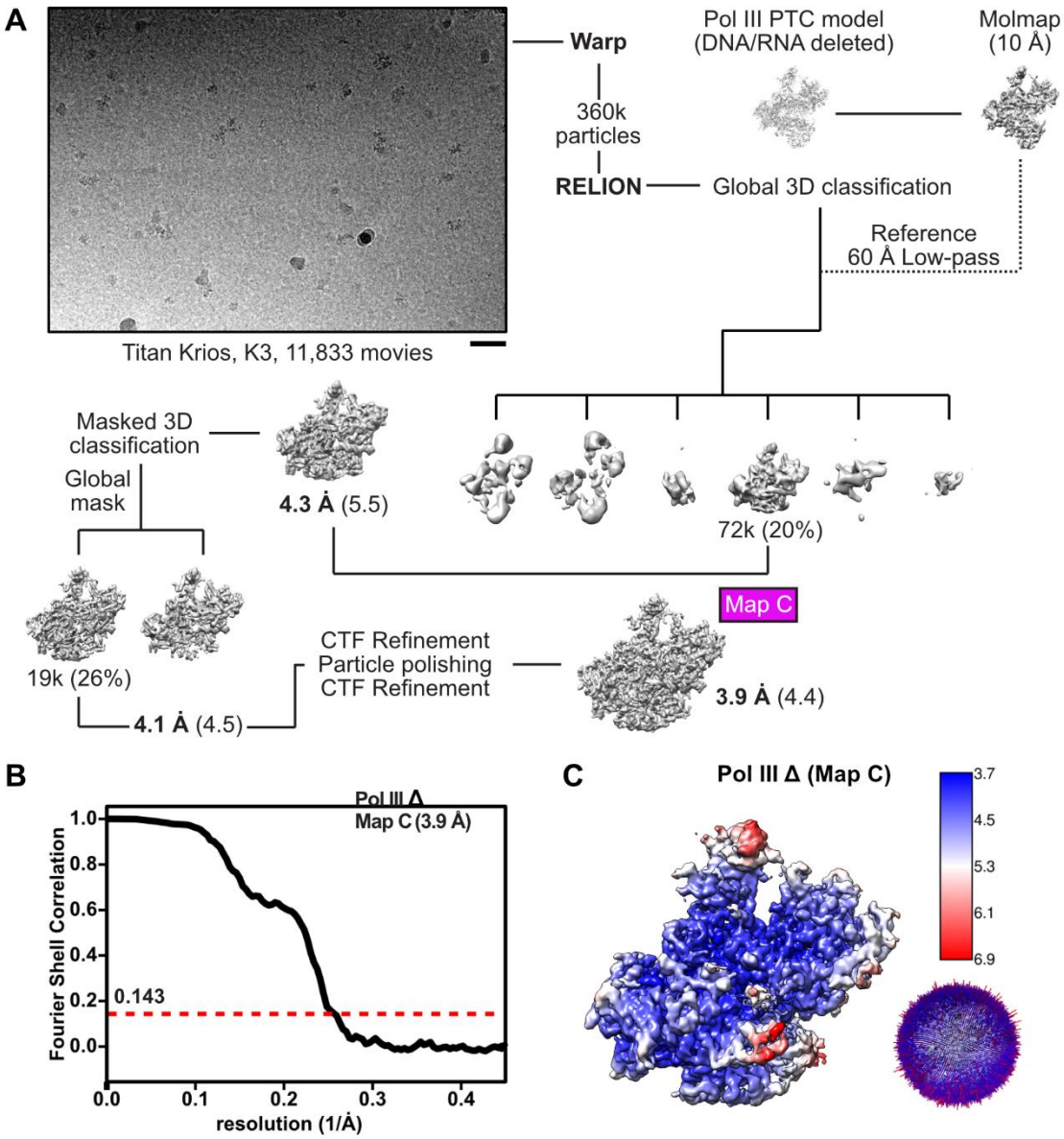

Data S3. Data-collection and -processing workflow of yeast Pol III Δ, Related to Figure 5.

(A) Cryo-EM data collection and processing strategy for the yeast Pol III Δ. Particle numbers are rounded down. Shown are the unsharpened cryo-EM maps obtain via 3D refinement in RELION. Reported resolution values are given below the cryo-EM maps and correspond to sharpened maps obtained via RELION post-processing. The resolution values of the unsharpened 3D maps are added in round brackets. Scale bar: 50 nm.

(B) Fourier shell correlation (FSC) curve of the yeast Pol III Δ derived via RELION post-processing (FSC = 0.143).

(C) Estimation of local resolution and angular distribution plot of the yeast Pol III Δ. Shown is the unsharpened cryo-EM map.

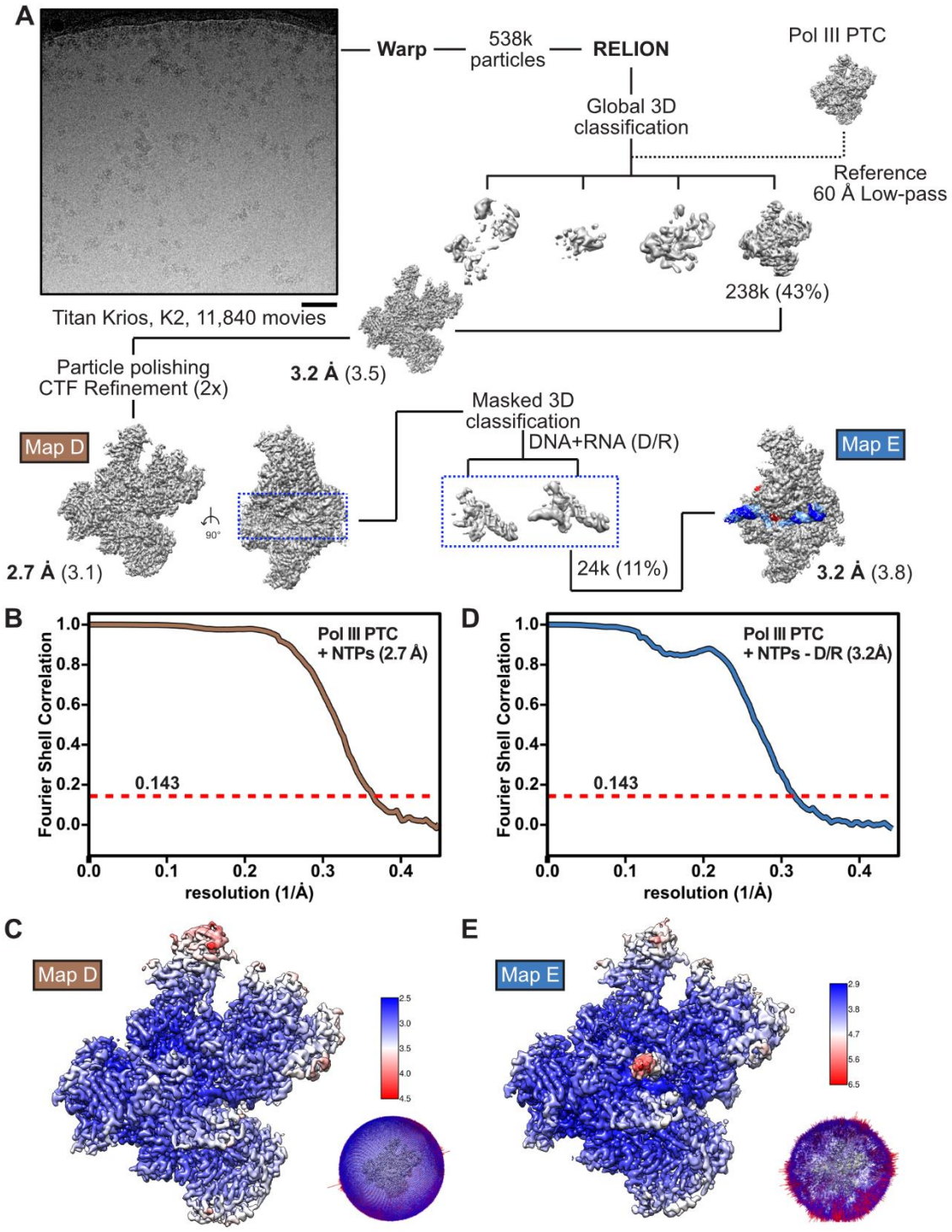

Data S4. Data-collection and -processing workflow of yeast Pol III PTC + NTPs, Related to Figure 6.

(A) Cryo-EM data collection and processing strategy for the yeast Pol III PTC + NTPs. Particle numbers are rounded down. Shown are the unsharpened cryo-EM maps obtain via 3D refinement in RELION. Reported resolution values are given below the cryo-EM maps and correspond to sharpened maps obtained via RELION post-processing. The resolution values of the unsharpened 3D maps are added in round brackets. Map features that show improved cryo-EM signal after masked 3D classification are highlighted in colours. Scale bar: 50 nm.

(B) Fourier shell correlation (FSC) curve of the yeast Pol III PTC + NTPs derived via RELION post-processing (FSC = 0.143).

(C) Fourier shell correlation (FSC) curve of the yeast Pol III PTC + NTPs map that was subjected to masked 3D-classification on the bound DNA/RNA (D/R) elements.

(D) Estimation of local resolution and angular distribution plot of the yeast Pol III PTC + NTPs. Shown is the unsharpened cryo-EM map.

(E) Estimation of local resolution and angular distribution plot of the yeast Pol III PTC + NTPs classified on the DNA/RNA elements. Shown is the unsharpened cryo-EM map.

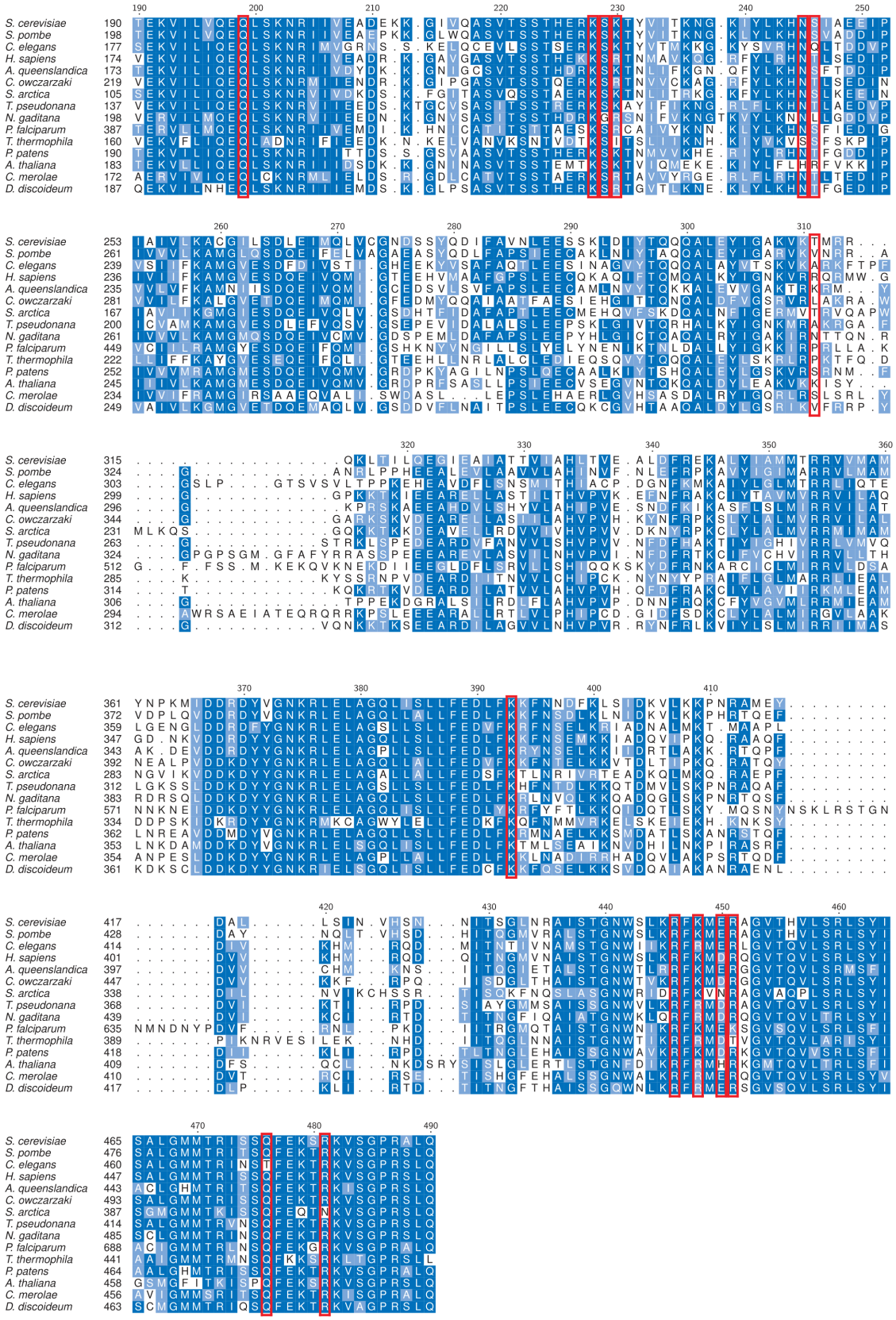

Data S5, Related to Figure 2, D. Multiple sequence alignment of subunit RPC2 (C128). The sequence range is 190 to 490 in *S. cerevisiae*. Residues that form H-bonds with the NT-strand are highlighted in red.

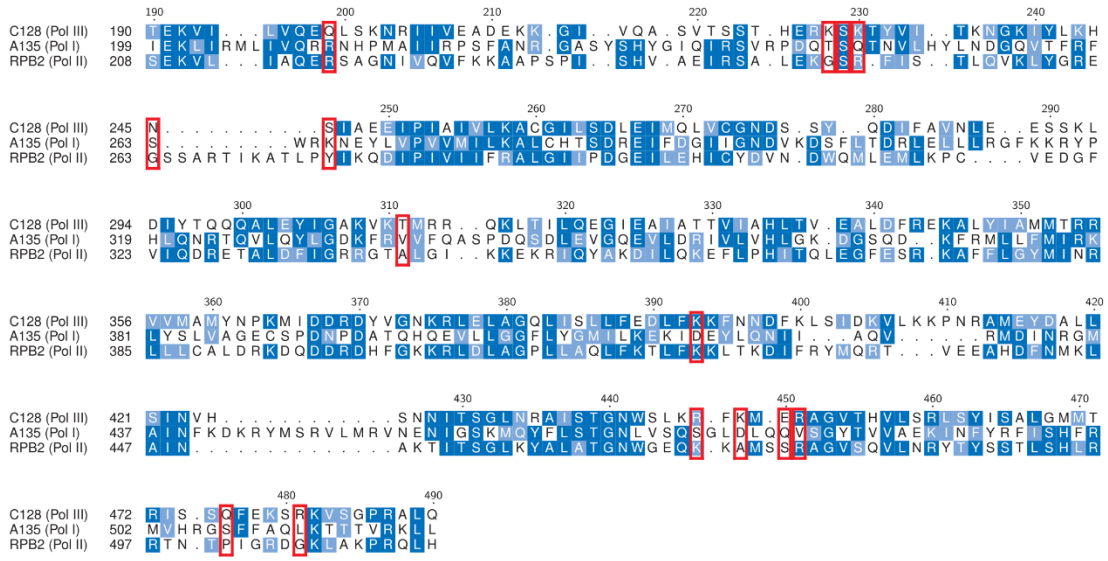

Data S6, Related to Figure 2, E. Multiple sequence alignment of *S. cerevisiae* C128 (Pol III) and its paralogs A135 (Pol I) and RBP1 Pol II. The sequence range is 190 to 490 in C128. Residues that form H-bonds with the NT-strand in the Pol III PTC are highlighted in red.